Mesh-free hydrodynamic stability

Tianyi Chu, Oliver T. Schmidt *

Department of Mechanical and Aerospace Engineering, University of California San Diego, 9500 Gilman Drive, La Jolla, CA 92093, USA

ARTICLE INFO

ABSTRACT

A specialized mesh-free radial basis function-based finite difference (RBF-FD) discretization is used to solve the large eigenvalue problems arising in hydrodynamic stability analyses of flows in complex domains. Polyharmonic spline functions with polynomial augmentation (PHS+poly) are used to construct the discrete linearized incompressible and compressible Navier-Stokes operators on scattered nodes. Rigorous global and local eigenvalue stability studies of these global operators and their constituent RBF stencils provide a set of parameters that guarantee stability without the need for hyperviscosity or other ad hoc regularizations, while balancing accuracy and computational efficiency. Specialized elliptical stencils to compute boundary-normal derivatives are introduced, and the treatment of reflectional and rotational symmetries is discussed. In particular, treating the pole singularity in cylindrical coordinates permits dimensionality reduction from 3D to 2D in rotational flows like jets. The numerical framework is demonstrated and validated on several hydrodynamic stability methods ranging from classical linear theory of laminar flows to state-of-the-art non-modal approaches that are applicable to turbulent mean flows. The examples include linear stability, resolvent, and wavemaker analyses of cylinder flow at Reynolds numbers ranging from 47 to 180, and resolvent and wavemaker analyses of the self-similar flat-plate boundary layer at a Reynolds number as well as the turbulent mean of a high-Reynolds-number transonic jet at Mach number 0.9. All previously-known results are found in close agreement with the literature. Finally, the resolvent-based wavemaker analyses of the Blasius boundary layer and turbulent jet flows offer new physical insight into the modal and non-modal growth in these flows.

1. Introduction

Flow instabilities and large-scale coherent structures are ubiquitous phenomena in fluid mechanics that have been the focus of extensive research. Linear stability (LST) analysis is specifically designed to investigate the growth of small perturbations exclusively around laminar base flows, which are the steady-state solution to the Navier-Stokes equations. One-dimensional LST analysis was widely used in the past century, e.g., [18,28,49,75]. Eriksson and Rizzi [33] and Tuckerman and Marcus [137] were the pioneers in conducting LST analysis in two-dimensional (2D). Subsequently, Jackson [54] and Zebib [147] examined the 2D nature of vortex shedding in the wakes of bluff bodies. Readers are referred to Huerre and Monkewitz [50] and Theofilis [127] for comprehensive reviews of the concept of 2D LST modes. The implementation of the 2D LST framework has enabled improved identification of flow instability in non-parallel flows, including cylinder wakes [43,72,85], aerofoil wakes [31,144], boundary layers [1,32], and jets in cross-flow [9,89,101]. Studies have demonstrated that an open flow can possess marginal stability despite exhibiting local convective

instability. LST analysis around a steady laminar base flow, by its inherent nature, is not applicable to predict finite-amplitude flow instabilities arising from nonlinear interactions. The use of mean flow for LST analysis, despite violating the basic assumption of linear theory, has been used successfully to predict coherent flow features in diverse types of flows, including cylinder wakes [10,94], open cavity flows [118,119], mixing layers [42,83,142], and turbulent or transitional jets [45,86,108]. Theoretical conditions required for the validity of mean flow stability analysis have been explored by Beneddine et al. [17]. Although beyond the scope of this work, it is noteworthy that the weakly-nonlinear extension of LST analysis has been successfully employed for studying the dynamics of non-parallel flows [25,119]. The LST-based semi-empirical e^N method [52,123] has succeeded in transition prediction for certain flows such as boundary layers. However, the prediction of disturbance behavior in more complex scenarios, such as crossflows or bypass transitions, falls outside the scope of LST theory.

Despite these limitations, resolvent, or input-output analysis, has recently emerged as a linear tool for accurately predicting large-scale coherent structures in fully turbulent flows. Resolvent analysis (RA) originally stems from the studies of transient growth [34,98,99,135] and seeks the optimal pairs of inputs and corresponding outputs through the linearized system that maximizes the energy gain. Within the laminar regime, RA has been utilized to investigate the linear response to external body forces or perturbations for channel flows [61,80,105], boundary layers [4,19,22,84,91,120,133], and jets [41,56,110]. In contrast to classical LST analysis, the input-output perspective offers a mathematically rigorous framework for studying turbulent mean-flows by identifying the forcing as the Reynolds stresses in the perturbation-interaction terms in the Reynolds-decomposed Navier–Stokes equations [77,116]. Applications include near-wall flows [51,1,116], boundary layers [5,55,104], incompressible [41,66] or compressible jets [56,109,134], and airfoil wakes [102,146]. The validation of fundamental relationships between RA and other modal decomposition techniques was facilitated by Towne et al. [134], establishing RA as a well-suited tool for turbulence modeling [92,93]. Both classical LST and RA require, in their most basic form, the construction of large matrices that have to be decomposed into their singular- or eigen-components. The construction and decomposition of these matrices are particularly challenging for flows in complex geometries. Previous studies [30,103,117,146] have leveraged the flexibility of the finite-volume (FV) methods on unstructured meshes. However, a downside of unstructured FV methods is that the accuracy is usually restricted to 2nd-order. Alternatively, the utilization of finite-element (FE) methods for spatial discretization provides high-order accuracy for flow instability analysis [72,73,104,119]. The commonly employed weak formulation of governing equations in FE methods raises concerns regarding stability and convergence. Finite-element (FE) methods offer the same flexibility, and the FreeFEM+ toolbox by Hecht [48] has been employed in a number of recent studies [72,73,104,119]. Matrix-free methods, such as the time-stepper [6,9,136] and other related techniques [29,74,84,87], provide an alternative approach where the decomposition of large matrix operations can be completely circumvented. Iterative Krylov subspace methods are commonly employed to obtain a partial eigendecomposition. However, their major limitation lies in their capacity to extract only a limited portion of the spectra at a time. Randomized approaches have also been explored as potential solutions to decrease the computational cost of the singular- or eigendecomposition of large stability matrices [81,102]. In this study, we demonstrate the capability and accuracy of radial basis functions (RBF) in effectively addressing the aforementioned challenges.

The use of RBF-based methods provides high flexibility in meshing complex geometries, allowing for local grid refinement and local adjustments to the order of accuracy of the discretization. The RBF methodology is rooted in scattered data interpolation, first introduced by Hardy [47], and offers a systematic means of approximating multivariate functions on arbitrarily scattered nodes. By generalizing the classical finite-difference (FD) methods, the so-called RBF-FD methods enable the approximation of spatial derivatives to arbitrary node layouts based on RBFs [130]. In fluid flow problems, Gaussian (GA), multiquadric (MQ), and inverse multiquadric (IMQ) are among the most commonly used radial basis functions (RBFs). Refer to Fornberg and Flyer [39] for a detailed overview. The computation of these RBFs requires specifying a shape parameter, a free parameter that can significantly impact both the numerical stability and accuracy. Recently, a new class of RBF-FD approximations has emerged that utilizes polyharmonic splines (PHS) augmented with polynomials (PHS+poly). This technique was first introduced by Flyer et al. [36] and has demonstrated great potential in achieving high-order accuracy while avoiding the difficulties associated with the shape parameter selection. Bayona et al. [14] and Flyer et al. [37] highlighted the advantages of local PHS+poly-generated RBF-FD stencils in achieving high-order accuracy for derivative approximations and solving elliptic partial differential equations (PDEs), while also eliminating stagnation errors under node refinement. The feasibility of implementing a larger stencil near domain boundaries to avoid the Runge phenomenon was analytically verified by Bayona [12] using RBFs in a closed-form. Additional numerical examples in 2-D and 3-D were presented in Bayona et al. [15] to demonstrate the effectiveness of the PHS+poly approach. The accuracy and stability of the PHS+poly RBF-FD method depend on the combination of the stencil size, PHS exponent, and the degree of polynomials. Several studies, including Chu and Schmidt [27], Le Borne and Leinen [64], Shankar and Fogelson [115], have investigated and discussed the optimal combinations of these parameters to achieve the 'spectral-like' accuracy of higher-order Padé-type compact FDs [65]. In addition, other approaches have been explored to improve the computational accuracy and efficiency of PHS+poly RBF-FDs, including overlapping stencils [114,115], the partition of unity (PU) method [79], and oversampling [131]. Comparative analyses have been carried out on various higher-order mesh-free discretizations, consistently demonstrating that PHS+poly-based RBF-FDs outperform other methods in accuracy, robustness, and computational efficiency, e.g., [13,37,44,88,106]. Recent successful applications of PHS+poly RBF-FDs in flow simulations on scattered nodes [111–113,138] highlight the potential of RBF methods for investigating flow instabilities in complex geometries. In our recent work [27], we introduced a staggered-node RBF-FD-based semi-implicit fractional-step solver for the incompressible Navier-Stokes equations, which will be utilized to compute the base state in the present study.

This work introduces a high-order, mesh-free framework for hydrodynamic stability analysis based on the PHS+poly RBF-FD discretizations. The efficient construction of global Jacobians on scattered nodes using RBF-based methods is demonstrated. The trade-off between computational efficiency and accuracy is addressed, and best practices are provided. Furthermore, we discuss

the practical treatment of boundary conditions, particularly the boundary-normal derivatives and the pole singularity in cylindrical coordinates. The numerical framework is demonstrated on various hydrodynamic stability theoretical methods and flows. Refer to Table 3 for an overview. In particular, LST, RA, and wavemaker (WM) analyses are shown for the canonical cylinder flow at Reynolds numbers ranging from 47 to 180, RA and WM analyses for a laminar zero-pressure-gradient (ZPG) flat-plate Blasius boundary layer at a Reynolds number of 6×10^5, RA and WM analyses for a turbulent transonic jet at Mach number 0.9 and a Reynolds number of approximately 10^6. The identified flow phenomena include vortex shedding in cylinder wakes [10,94], the Orr and Tollmien-Schlichting waves in boundary layers [1,20,84,120], and Orr and Kelvin-Helmholtz wavepackets [24,41,66,109,125] as well as trapped acoustic waves [108,132] in turbulent jets. The comparisons of these benchmark problems with the literature allow us to highlight the viability, accuracy, and robustness. The study furthermore encapsulates the first application of RA-based WM analysis to the ZPG Blasius boundary layer and turbulent jets, providing a new perspective on modal and non-modal growth in these flows.

This paper is organized as follows: §2 introduces the PHS+poly RBF-FD method, §3 presents the mesh-free hydrodynamic stability analysis, and §4 discusses the numerical implementations. The performance of the mesh-free framework is demonstrated in §5. Finally, §6 concludes and summarizes the paper.

2. Radial basis function-based finite differences (RBF-FD)

The goal of the RBF-FD method is to compute the discrete representation of any linear differentiation operator $\mathcal{D}$ at a given location x_0 as a linear combination of the function values $g(\boldsymbol{x}_j)$, such that

$$\mathcal{D}g(\boldsymbol{x}_0) \approx \sum_{j=1}^{n} w_j g(\boldsymbol{x}_j). \tag{1}$$

To obtain the unknown differentiation weights w_j, we use the RBF interpolant,

$$s(\boldsymbol{x}) = \sum_{j=1}^{n} \gamma_j \phi(\|\boldsymbol{x} - \boldsymbol{x}_j\|), \tag{2}$$

to approximate the given function $g(\boldsymbol{x})$ by satisfying

$$s(\boldsymbol{x}_j) = g(\boldsymbol{x}_j), \qquad j = 1, 2, \cdots n. \tag{3}$$

Here, $\phi(r)$ is a smooth radial function, $\{\boldsymbol{x}_j\}_{j=1}^{n}$ is a set of scattered nodes, and $\|\cdot\|$ denotes the standard Euclidean norm. Combining equations (1)-(3) leads to the linear system

$$\underbrace{\begin{bmatrix} \phi(\|\boldsymbol{x}_1 - \boldsymbol{x}_1\|) & \phi(\|\boldsymbol{x}_1 - \boldsymbol{x}_2\|) & \cdots & \phi(\|\boldsymbol{x}_1 - \boldsymbol{x}_n\|) \\ \phi(\|\boldsymbol{x}_2 - \boldsymbol{x}_1\|) & \phi(\|\boldsymbol{x}_2 - \boldsymbol{x}_2\|) & \cdots & \phi(\|\boldsymbol{x}_2 - \boldsymbol{x}_n\|) \\ \vdots & \vdots & & \vdots \\ \phi(\|\boldsymbol{x}_n - \boldsymbol{x}_1\|) & \phi(\|\boldsymbol{x}_n - \boldsymbol{x}_2\|) & \cdots & \phi(\|\boldsymbol{x}_n - \boldsymbol{x}_n\|) \end{bmatrix}}_{\boldsymbol{A}} \begin{bmatrix} w_1 \\ w_2 \\ \vdots \\ w_n \end{bmatrix} = \begin{bmatrix} \mathcal{D}\phi(\|\boldsymbol{x} - \boldsymbol{x}_1\|)\big|_{\boldsymbol{x}=\boldsymbol{x}_0} \\ \mathcal{D}\phi(\|\boldsymbol{x} - \boldsymbol{x}_2\|)\big|_{\boldsymbol{x}=\boldsymbol{x}_0} \\ \vdots \\ \mathcal{D}\phi(\|\boldsymbol{x} - \boldsymbol{x}_n\|)\big|_{\boldsymbol{x}=\boldsymbol{x}_0} \end{bmatrix}, \tag{4}$$

which can be solved directly to obtain the weight vector $\boldsymbol{w} = [w_1, \cdots, w_n]^T$. An implicit assumption for equation (4) is that the derivative of the basis function, $\mathcal{D}\phi$, is continuous.

Polynomial augmentation is commonly applied to the RBF-FD method to enforce consistency with Taylor expansion-based FD approximations [36,39,40,63,145]. The two-dimensional augmented RBF-FD method can be expressed as

$$\mathcal{D}g(\boldsymbol{x}_0) \approx \sum_{j=1}^{n} w_j g(\boldsymbol{x}_j) + \sum_{i=1}^{(q+1)(q+2)/2} c_i P_i(\boldsymbol{x}_0), \tag{5}$$

where $\{P_i(\boldsymbol{x})\}$ are multivariate polynomials up to degree q. Taking Cartesian coordinates as an example, $P_i(\boldsymbol{x})$ represents the ith element in the multivariate polynomial series $\{1, x, y, x^2, xy, y^2, \cdots\}$. To match the local Taylor series, additional constraints for the differentiation weights,

$$\sum_{j=1}^{n} w_j P_i(\boldsymbol{x}_j) = \mathcal{D}P_i(\boldsymbol{x}_0) \qquad \text{for } 1 \le i \le \frac{(q+1)(q+2)}{2}, \tag{6}$$

are included in the computation. These constraints, also referred to as the vanishing momentum conditions [53], ensure that the RBF approximations locally reproduce polynomial behavior up to degree q [37] and decay in the far-field [38]. A more general and compact representation of equations (5)-(6) are

$$\underbrace{\begin{bmatrix} \boldsymbol{A} & \boldsymbol{P} \\ \boldsymbol{P}^T & \boldsymbol{0} \end{bmatrix}}_{\boldsymbol{A}_{\text{aug}}} \begin{bmatrix} \boldsymbol{w} \\ \boldsymbol{c} \end{bmatrix} = \begin{bmatrix} \mathcal{D}\boldsymbol{\phi} \\ \mathcal{D}\boldsymbol{P} \end{bmatrix}, \tag{7}$$

Table 1
Summary of flow state decompositions.

Base state	Description	Notation	Obtained from	Remaning forcing f'
$(\boldsymbol{u}_0, p_0)$	Base flow	$(\boldsymbol{U}, P)$	equation (11)	$-\left(\boldsymbol{u}' \cdot \nabla\right) \boldsymbol{u}'$
	Mean flow	$(\overline{\boldsymbol{u}}, \overline{p})$	long-time average	$-\left(\boldsymbol{u}' \cdot \nabla\right) \boldsymbol{u}' + \overline{\left(\boldsymbol{u}' \cdot \nabla\right) \boldsymbol{u}'}$

where $\boldsymbol{A}$ represents the same interpolation matrix as defined in equation (4). In equation (1), only the weight vector $\boldsymbol{w}$ is used to approximate the differentiation operator D. Motivated by recent studies (see, e.g., [14,15,36,37]), we use polyharmonic splines (PHS),

$$\phi(r) = r^m, \tag{8}$$

as the basis functions, where m is an odd positive integer. The accuracy and stability of this PHS+poly RBF-FD method depend on the combination of the stencil size, PHS exponent, and the degree of polynomials. The selection of these parameters will be discussed later in §4.1.

RBF-FD methods provide a mesh-free approach for discretizing the domain without the need for a pre-defined mesh or explicit node connectivity. This feature enables the investigation of flow instabilities for complex geometries, thereby offering advantages over traditional discretizations that rely on structured meshes. The subsequent sections of this paper focus on the construction of the discrete linearized Navier-Stokes (LNS) and then the resolvent operators using PHS+poly RBF-FDs.

3. Mesh-free hydrodynamic stability analysis

3.1. Governing equations

The motion of a general incompressible Newtonian fluid is governed by the Navier-Stokes equations,

$$\frac{\partial \boldsymbol{u}}{t} + (\boldsymbol{u} \cdot \nabla) \boldsymbol{u} = -\nabla p + \text{Re}^{-1} \nabla^2 \boldsymbol{u}, \tag{9a}$$

$$\nabla \cdot \boldsymbol{u} = 0. \tag{9b}$$

Here, all variables are nondimensionalized by the velocity scale $\boldsymbol{U}_\infty$ and the length scale L, and Re denotes the Reynolds number.

In the case of laminar flows, we can decompose the flow state around the steady-state solution of the Navier-Stokes equations (9) as

$$\boldsymbol{u} = \boldsymbol{U} + \boldsymbol{u}', \quad p = P + p', \tag{10}$$

where $(\boldsymbol{U}, P)$ represents the base flow that satisfies

$$(\boldsymbol{U} \cdot \nabla) \boldsymbol{U} = -\nabla P + \text{Re}^{-1} \nabla^2 \boldsymbol{U}, \tag{11a}$$

$$\nabla \cdot \boldsymbol{U} = 0, \tag{11b}$$

and $(\cdot)'$ denotes the small fluctuating components. In turbulent flows, we take the Reynolds decomposition of the flow state into the temporal mean, $\overline{(\cdot)}$, and fluctuating components, given by

$$\boldsymbol{u} = \overline{\boldsymbol{u}} + \boldsymbol{u}', \quad p = \overline{p} + p'. \tag{12}$$

By generalizing the notation of the base state as $(\boldsymbol{u}_0, p_0)$, the resulting governing equations for the fluctuations take the form of

$$\frac{\partial \boldsymbol{u}'}{t} + \left(\boldsymbol{u}_0 \cdot \nabla\right) \boldsymbol{u}' + \left(\boldsymbol{u}' \cdot \nabla\right) \boldsymbol{u}_0 = -\nabla p' + \text{Re}^{-1} \nabla^2 \boldsymbol{u}' + \boldsymbol{f}', \tag{13a}$$

$$\nabla \cdot \boldsymbol{u}' = 0. \tag{13b}$$

Here, the term $\boldsymbol{f}'$ represents the remaining nonlinear interactions between the fluctuation components. Table 1 summarizes the two aforementioned decompositions.

Equation (13) can be written compactly in terms of the fluctuating state, $\boldsymbol{q}' = [u', v', p']^T$, as

$$\mathcal{P}\mathcal{P}^T \left(\frac{\partial}{t} \boldsymbol{q}'\right) = \mathcal{L} \boldsymbol{q}' + \mathcal{P} \boldsymbol{f}', \tag{14}$$

where $\mathcal{P}$ is the prolongation operator that extends the velocity vector $[u, v]^T$ into $[u, v, 0]^T$, and its transpose is the restriction operator that extracts the velocity vector from the extended state vector [120]. The incompressible linearized Navier-Stokes (LNS) operator takes the form of

$$\mathcal{L} \equiv \begin{pmatrix} -\left(\boldsymbol{u}_0 \cdot \nabla\right)() - [()\cdot \nabla] \boldsymbol{u}_0 + \text{Re}^{-1} \nabla^2 & -\nabla \\ \nabla \cdot () & 0 \end{pmatrix}. \tag{15}$$

The governing equations for compressible flows will be discussed in §5.3 and Appendix A. Beyond the linear dynamics, the remaining forcing f' in equation (14) comprises products of fluctuating quantities, as outlined in Table 1. These terms will be either neglected or modeled.

Classical (temporal) linear stability (LST) analysis investigates fluctuations with complex frequency $\lambda = \lambda_r + i\lambda_i$, where λ_r is the exponential growth rate and λ_i the oscillation frequency. The fluctuations are assumed to be infinitesimally small, and the forcing term, f', is, therefore, negligible at $O(1)$, see, e.g., Schmid and Henningson [107]. Substituting perturbations of the form $q'(x,t) = \tilde{q}(x)e^{\lambda t}$ into the governing equations (13) yields the LST equation,

$$\lambda \mathcal{P}\mathcal{P}^T \tilde{q} = \mathcal{L}\tilde{q}. \tag{16}$$

Equation (16) is a generalized eigenvalue problem, and the eigenvector associated with the largest growth rate ought to predict the dominant flow instability mechanism.

The nonlinear interactions in equation (14) are no longer negligible for general cases of finite amplitude fluctuations. Within the resolvent framework of turbulent flows, the nonlinear interactions, along with the background turbulence, can be interpreted as external forcing, f', to the otherwise linear dynamics. This interpretation was first proposed by McKeon and Sharma [77]. By assuming a normal mode form for the fluctuating components,

$$[u', q', f'](x,t) = [\hat{u}, \hat{q}, \hat{f}](x)e^{i\omega t} + c.c., \tag{17}$$

where ω is the angular frequency, or equivalently by taking the Fourier transform, we obtain the linear time-invariant (LTI) representation of the governing equation (13) in the frequency domain,

$$\left(i\omega \mathcal{P}\mathcal{P}^T - \mathcal{L}\right)\hat{q} = \mathcal{P}\left(\mathcal{B}\hat{f}\right), \tag{18a}$$

$$\hat{u} = \mathcal{P}^T\left(\mathcal{C}\hat{q}\right). \tag{18b}$$

The linear operators $\mathcal{B}$ and $\mathcal{C}$ are used to select spatial regions of particular interest. We write equations (18) in a compact form as

$$\hat{u} = \mathcal{H}(\omega)\hat{f}, \tag{19}$$

where $\mathcal{H}(\omega) = \mathcal{P}^T \mathcal{C} \left(i\omega \mathcal{P}\mathcal{P}^T - \mathcal{L}\right)^{-1} \mathcal{P}\mathcal{B}$ is known as the resolvent operator. The numerical discretization of the global operator, $\mathcal{L}$, is at the core of both LST and resolvent analyses. In this work, the PHS+poly RBF-FDs are utilized to construct differentiation matrices and global Jacobians on scattered nodes, taking advantage of their flexibility and accuracy in numerical discretization.

3.2. Global Jacobians and mesh-free stability analysis

For differentiation operators $\mathcal{D} = \frac{\partial^{(\alpha+\beta)}}{\partial x_1^\alpha \partial x_2^\beta}$ with $\alpha + \beta \leq 2$, we seek sparse differentiation matrices $D_{x_1^\alpha x_2^\beta}$ that satisfy

$$\underbrace{\begin{bmatrix} \text{---} w_1^T \text{---} \\ \text{---} w_2^T \text{---} \\ \vdots \\ \text{---} w_N^T \text{---} \end{bmatrix}}_{D_{x_1^\alpha x_2^\beta}} \begin{bmatrix} g(x_1) \\ g(x_2) \\ \vdots \\ g(x_N) \end{bmatrix} \approx \begin{bmatrix} \frac{\partial^{(\alpha+\beta)}}{\partial x_1^\alpha \partial x_2^\beta} g(x)\big|_{x=x_1} \\ \frac{\partial^{(\alpha+\beta)}}{\partial x_1^\alpha \partial x_2^\beta} g(x)\big|_{x=x_2} \\ \vdots \\ \frac{\partial^{(\alpha+\beta)}}{\partial x_1^\alpha \partial x_2^\beta} g(x)\big|_{x=x_N} \end{bmatrix}. \tag{20}$$

Here, (x_1, x_2) represents the coordinate system, and $\{x_i\}_{i=1}^N$ represents the global computational grid. The jth row of the sparse matrix D, denoted as w_j^T, contains the $n \ll N$ non-zero weights that approximate the derivative at node x_j. The matrix hence has $N \times n$ nonzero elements. For example, with the best-practice values later listed in Table 2, the sparsity of the differentiation operators exceeds 99.97%. In a slight change of notation, to enhance readability, we now denote by $u = u(x)$ and $v = v(x)$ the global velocity fields, and by $p = p(x)$ the global pressure field in the computational domain Ω.

Upon the use of these global RBF-FD-based differentiation matrices, we assemble the discrete global LNS operator from equation (15), taking the two-dimensional Cartesian coordinate system as an example, as

$$L = \begin{pmatrix} S - \text{diag}\left(D_x u_0\right) + \text{Re}^{-1}\left(D_{xx} + D_{yy}\right) & -\text{diag}\left(D_y u_0\right) & -D_x \\ -\text{diag}\left(D_x v_0\right) & S - \text{diag}\left(D_y v_0\right) + \text{Re}^{-1}\left(D_{xx} + D_{yy}\right) & -D_y \\ D_x & D_y & 0 \end{pmatrix}, \tag{21}$$

where $S = -\left(u_0 \circ D_x + v_0 \circ D_y\right)$, and $\circ$ denotes the Hadamard product.

For a weighted inner product $\langle q_1, q_2 \rangle = q_2^* W q_1$ that accounts for the non-uniformly distributed nodes, the discrete LST and its adjoint eigenvalue problems take the form of

$$\lambda P P^T \tilde{q} = L\tilde{q}, \tag{22a}$$

$$\lambda^+ P P^T \tilde{q}^+ = L^+ \tilde{q}^+, \tag{22b}$$

respectively, where

$$L^+ = W^{-1} L^H W \tag{23}$$

is the discrete adjoint LNS operator. Here, the restriction matrix for two-dimensional problems takes the form of $P^T = \begin{bmatrix} I & 0 & 0 \\ 0 & I & 0 \end{bmatrix}$, and $(\cdot)^H$ denotes the Hermitian transpose. The eigenvectors of these two generalized eigenvalue problems, $\tilde{q} = [\tilde{u}, \tilde{v}, \tilde{p}]^T$ and $\tilde{q}^+ = [\tilde{u}^+, \tilde{v}^+, \tilde{p}^+]^T$, are referred to as the LST and adjoint modes, respectively.

The wavemaker (WM), introduced by Giannetti and Luchini [43], identifies the flow region with the strongest localized feedback, where the dominant instability mechanisms act. Based on the leading LST and adjoint modes, the WM is locally defined as

$$\zeta_{\text{LST}}(x_1, x_2) = \frac{\|P^T \tilde{q}^+(x_1, x_2)\| \, \|P^T \tilde{q}(x_1, x_2)\|}{|\langle \tilde{q}^+, \tilde{q} \rangle|}, \tag{24}$$

where the norm $\| \cdot \|$ measures the localized energy. Referred to Luchini and Bottaro [67] for a comprehensive review. In addition to quantifying the receptivity, the wavemaker also indicates the non-normality level of the flow field [25]. Initially introduced for base flows, Meliga et al. [78] extended the application of wavemaker as a sensitivity analysis technique for mean flows. We utilize this methodology to gauge the structural sensitivity of the RBF-FD-based global LNS operator, L.

3.3. Mesh-free resolvent analysis (RA)

The construction of the global Jacobian, L, leads to the direct discretization of the input-output system in equation (19), yielding

$$\hat{u} = H(\omega)\hat{f}, \tag{25}$$

where

$$H(\omega) = P^T C \left(i\omega P P^T - L \right)^{-1} P B \tag{26}$$

is referred to as the discrete resolvent operator.

In the absence of nonlinear interactions described in table (1), the application of input-output, or resolvent analysis (RA) provides a means to model them as optimal forcing inputs to the linear system in equation (25). The objective of resolvent analysis is to identify pairs of optimal forcings and their corresponding responses that maximize the gain, σ^2, defined as the ratio of the energy of the response to the energy of the forcing,

$$\sigma^2(\hat{f}; \omega) = \frac{\|\hat{u}\|_u^2}{\|\hat{f}\|_f^2} = \frac{\left\langle H(\omega)\hat{f}, H(\omega)\hat{f} \right\rangle_u}{\left\langle \hat{f}, \hat{f} \right\rangle_f}. \tag{27}$$

Refer to Schmid and Henningson [107] for a detailed discussion. The energy of the response and the forcing are measured in the norms $\| \cdot \|_u$ and $\| \cdot \|_f$, induced by the inner products

$$\langle \hat{u}_1, \hat{u}_2 \rangle_u = \hat{u}_2^* W_u \hat{u}_1 \qquad \text{and} \qquad \left\langle \hat{f}_1, \hat{f}_2 \right\rangle_f = \hat{f}_2^* W_f \hat{f}_1 \tag{28}$$

on the output and input spaces, respectively. Here, W_u and W_f are weight matrices containing both the numerical quadrature weights and weights associated with these inner products.

We further define the modified, or weighted, resolvent operator

$$R(\omega) \equiv W_u^{\frac{1}{2}} H(\omega) W_f^{-\frac{1}{2}} = \hat{U} \Sigma \hat{F}^* \tag{29}$$

to account for the energy in the input and output spaces. The optimal responses $\hat{U} = [\hat{u}_1, \cdots, \hat{u}_N]$ and the corresponding forcings $\hat{F} = [\hat{f}_1, \cdots, \hat{f}_N]$ are obtained from the singular value decomposition (SVD) of the modified resolvent operator and ranked by the energy gains $\Sigma = [\sigma_1, \cdots \sigma_N]$. The resulting modes are orthogonal in their respective inner products, that is, $\left\langle \hat{u}_j, \hat{u}_k \right\rangle_u = \left\langle \hat{f}_j, \hat{f}_k \right\rangle_f = \delta_{jk}$. The optimal input and output modes are related through

$$R(\omega)\hat{f}_j = \sigma_j(\omega)\hat{u}_j, \tag{30}$$

which provides a physical interpretation of the singular values and vectors. In practice, the optimal input forcings, $\hat{f}_j$, are determined as the solutions of the eigenvalue problem

$$W_f^{-1} H(\omega)^* W_u H(\omega)\hat{f}_j = \sigma_j^2 \hat{f}_j, \tag{31}$$

where $W_f^{-1} H(\omega)^* W_u H(\omega)$ is Hermitian. The matrix inversion of $\left(i\omega P P^T - L \right)$ is solved using LU-factorization [120].

The RA-based wavemaker,

$$\zeta_{\text{RA}}(x_1, x_2) = \frac{\|\hat{u}_1(x_1, x_2)\| \, \|\hat{f}_1(x_1, x_2)\|}{|\hat{u}_1^* W_u \hat{f}_1|}, \tag{32}$$
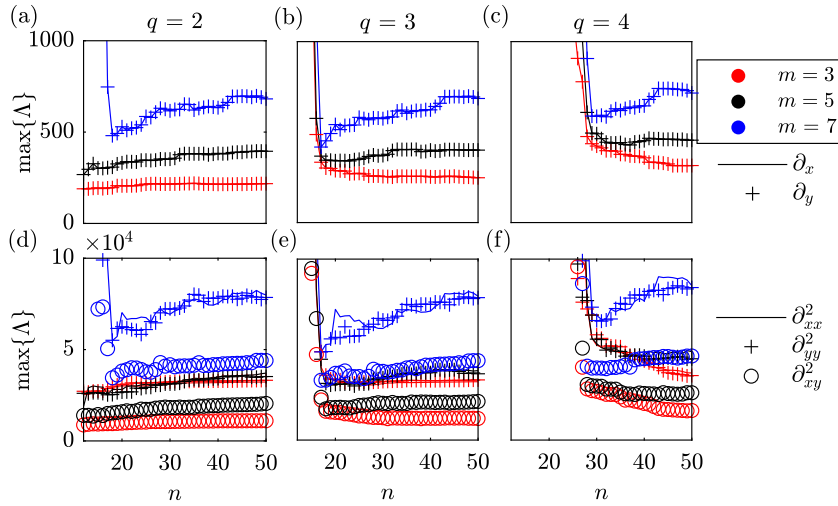
Fig. 1. Maximum local $\mathcal{L}$-Lebesgue function for different combinations of PHS exponents, m, and polynomial orders, q for the first (a-c) and second derivatives (d-f) in the x- (solid line), y- ('+') and xy-directions (circle).

is defined analogous to equation (24). Within the framework of RA, it provides a quantitative measure of the effect of the localized feedback at any given frequency [96,103,122,126].

4. Numerical implementations

4.1. Node generation and parameter selection

We employ the unstructured triangular mesh generator `DistMesh` developed by Persson [90] to efficiently generate scattered nodes with localized refinement in regions of interest. We highlight that the local connection information is not used in the computation. The accuracy and stability of the PHS+poly RBF-FD method are contingent upon three parameters: the stencil size, n, the PHS exponent, m, and the polynomial degree, q. We investigate the order of accuracy ranging from the standard choice of $q = 2$ to the desired high-order accuracy for hydrodynamic stability analysis, here $q = 4$. Increasing the order of accuracy generally leads to a decrease in the size of the linear operator.

The local $\mathcal{D}$-Lebesgue function proposed by Shankar and Fogelson [115] provides a measure of the eigenvalue stability of the RBF-FD method. For a given linear operator $\mathcal{D}$, the local Lebesgue function takes the form of the 1-norm of the RBF-FD weight in equation (1), that is

$$\Lambda_{\mathcal{D}}(\boldsymbol{x}_0; \{\boldsymbol{x}_j\}_{j=1}^n) = \|\boldsymbol{w}\|_1 = \sum_{j=1}^n |w_j|. \tag{33}$$

Larger values of the local Lebesgue function indicate an increased susceptibility to numerical instability in the assembled global differentiation matrix. Fig. 1 shows the maximum value of the local Lebesgue function across various parameter combinations based on the test grid shown in Fig. 4. Refer to the accompanying context of Fig. 4 for more details of the grid. For all considered stencil sizes, polynomial degrees, and relevant operators, the minimax value is consistently achieved at $m = 3$, suggesting its suitability for hydrodynamic stability analysis.

For two-dimensional problems, it has been suggested that the stencil size should satisfy $n \gtrsim (q+1)(q+2)$ [36,37]. In practice, including a few additional nodes beyond the minimum requirement is often beneficial to improve performance. The specific choice of additional nodes may depend on the type of node sets used. For instance, a recommended formula for Halton nodes is $n = (q+1)(q+2) + \lfloor \ln[(q+1)(q+2)] \rfloor$ [64,115]. We here select the stencil size n based on the assumption of a perfectly arranged hexagonal node distribution comprising $q/2 + 1$ layers, despite the actual distribution of nodes being heterogeneous. For practical examples, refer to Fig. 3 and the surrounding context. The recommended parameter combinations are summarized in Table 2. With these parameters, hyperviscosity or other means of regularization are not needed to stabilize the solution further. In particular, we use $(n, m, q) = (37, 3, 4)$ for interior nodes and $(n, m, q) = (19, 3, 2)$ for nodes near boundaries in the construction of the discrete LNS operator, $\boldsymbol{L}$. The RBF stencil for each node is determined as the nearest n nodes acquired through a k-nearest neighbor (kNN) search.

The condition number of the augmented matrix $\boldsymbol{A}_{\text{aug}}$, defined in equation (7), affects the numerical stability in a similar way and hence needs to be considered separately. The condition number for various parameter combinations has been investigated and discussed in Le Borne and Leinen [64]. Independent of the parameter selection, Shahane et al. [111] demonstrated that scaling the local stencil to a unit length scale can improve the condition number. We further reveal the existence of an optimal range for the averaged local grid spacing, wherein the condition number of the augmented matrix $\boldsymbol{A}_{\text{aug}}$ reaches its minimum value.

Table 2
Summary of parameter selections.

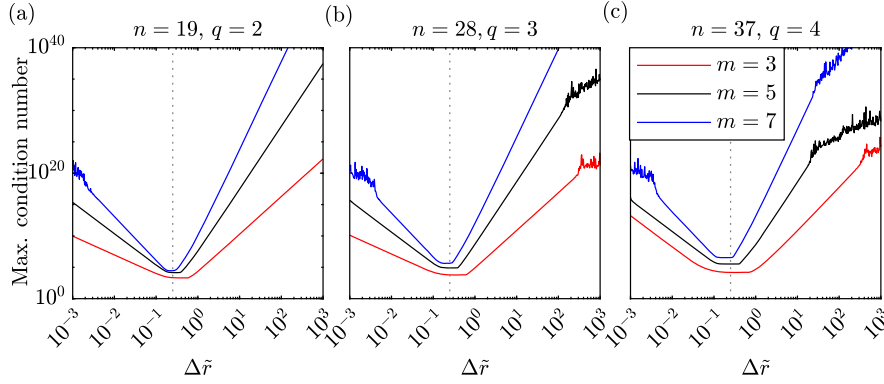|	Shankar and Fogelson [115]	Le Borne and Leinen [64]	present
$q = 2$	$(n, m) = (14, 3)$	$(n, m) = (14, 5)$	$(n, m) = (19, 3)$
$q = 3$	$(n, m) = (22, 3)$	$(n, m) = (22, 7)$	$(n, m) = (28, 3)$
$q = 4$	$(n, m) = (33, 3)$	$(n, m) = (33, 7)$	$(n, m) = (37, 3)$

Fig. 2. Maximum condition number of A_{aug} as a function of local grid spacing $\Delta \tilde{r}$: (a) $n = 19$, $q = 2$; (b) $n = 28$, $q = 3$; (c) $n = 37$, $q = 4$. The recommended local spacing of $\Delta \tilde{r} = 0.25$ is highlighted as dashed lines.

For a given stencil $\{x_j\}_{j=1}^n$, we perform scaling with respect to the location of x_0 with a scaling factor κ such that

$$\{\tilde{x}_j\}_{j=1}^n = \{\kappa(x_j - x_0)\}_{j=1}^n, \tag{34}$$

and the averaged local grid spacing becomes $\Delta \tilde{r} = \kappa \Delta r$. Fig. 2 shows the maximum condition number within the test grid as a function of $\Delta \tilde{r}$ for the considered parameters. Optimal performance is consistently achieved within the range of $0.15 \lesssim \Delta \tilde{r} \lesssim 0.3$ across all examined parameter combinations. Based on this, we perform spatial scaling to ensure an averaged local spacing of $\Delta \tilde{r} = 0.25$ before solving the RBF-FD weights in equation (1). The chain rule is applied to transform the RBF weights back to the original grid.

4.2. Boundary condition treatments

4.2.1. Homogeneous Dirichlet boundary conditions

Homogeneous Dirichlet boundary conditions, $q' = 0$, are widely employed in hydrodynamic stability analysis based on the assumption that perturbation variables either vanish at the solid wall or in the far field. Different methods to enforce Dirichlet boundary conditions in RBF-based [140,141] or other mesh-free collocation methods [97] have been proposed in the past. To approximate spatial derivatives for a node near such a boundary, we follow the Kansa method [62] and compute the RBF-FD weights using the local stencil consisting of both the interior nodes, $\{x^{(i)}\}_{j=1}^{n^{(i)}}$, and the boundary nodes, $\{x^{(b)}\}_{j=1}^{n^{(b)}}$. Letting $g(x_j^{(b)}) = 0$, equation (1) becomes

$$\mathcal{D}g(x_0) = \sum_{j=1}^{n^{(i)}} w_j^{(i)} g(x_j^{(i)}) + \sum_{j=1}^{n^{(b)}} w_j^{(b)} g(x_j^{(b)}) = \sum_{j=1}^{n^{(i)}} w_j^{(i)} g(x_j^{(i)}), \tag{35}$$

and only the weights for the interior nodes will be used in the computation.

4.2.2. Boundary-normal derivatives

Neumann conditions, inflow/outflow conditions, or the enforcement of continuity necessitate the evaluation of boundary-normal derivatives and require special treatment for scattered nodes that are not structured near boundaries. Using ghost nodes requires additional, generally non-physical, conditions for their evaluation. To avoid using ghost nodes and their associated computational overhead and implementation complexity, we propose the use of specialized stencils with boundary-normal alignment. To accurately approximate derivatives in the boundary-normal direction, we propose an elliptical stencil with its major axis perpendicular to the boundary. The elliptical form is achieved by utilizing a weighted Euclidean distance metric

$$\tilde{r} = \sqrt{a^2 + b^2} \sqrt{\frac{\left((x - x_0) \cdot n\right)^2}{a^2} + \frac{\left((x - x_0) \cdot t\right)^2}{b^2}}, \tag{36}$$

where n and t are the normal and tangential directions, respectively, and a and b denote the corresponding scaling factors. An eccentricity of $\frac{\sqrt{a^2 - b^2}}{a} = \frac{2\sqrt{6}}{5}$ is used in the computation. We use the $q = 2$ polynomial augmentation for the boundary-tangential
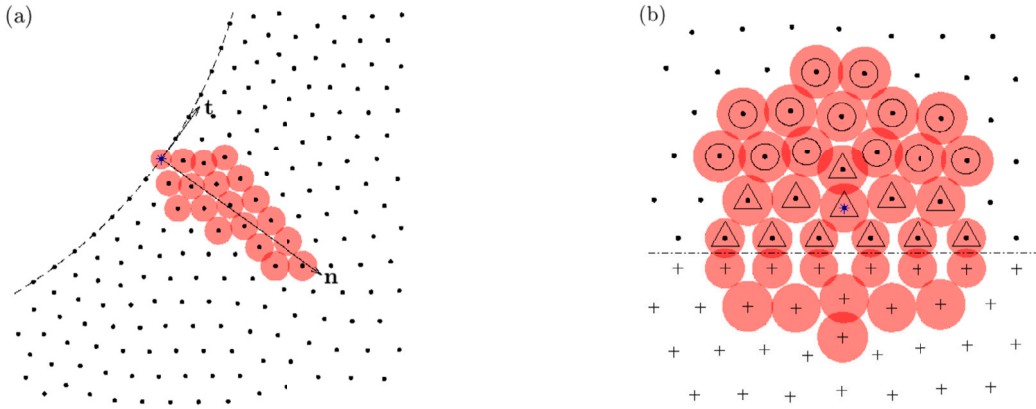
Fig. 3. RBF stencils (red-shaded circles) for a given node (blue star): (a) boundary-normal derivatives; (b) interior node near the symmetric centerline (dot-dashed). The latter stencil includes the interior nodes ($\{x^\bullet\}_{j=1}^{n^\bullet}$, dot) and image ghost nodes ($\{x^+\}_{j=1}^{n^+}$, '+'). The counterparts of the image nodes, $\{x^\Delta\}_{j=1}^{n^+}$, and the remaining nodes, $\{x^\circ_j\}_{j=1}^{n^\bullet-n^+}$, are shown as triangles and circles, respectively. The area of each red-shaded circle represents the corresponding local radial control volume, dV_i. (For interpretation of the colors in the figure(s), the reader is referred to the web version of this article.)

direction and a higher-order of accuracy of $q = 4$ for the boundary-normal direction. An illustrative example is shown in Fig. 3(a). This new strategy circumvents the need to increase the local stencil near domain boundaries to prevent the Runge phenomenon [12,14]. Without this special treatment, a significantly larger stencil size will be needed to attain stable solutions.

4.2.3. Symmetric and anti-symmetric boundary conditions

Exploiting physical and geometrical symmetries in flow problems leads to drastic computational savings. For example, a problem with simple reflectional symmetry will reduce the size of the linearized stability and resolvent operators to 25% of that in the full problem. This is particularly important for the direct solutions of eigen- and singular-value problems, for which memory is the bottleneck. For axisymmetric problems, like the jet problem at hand, the saving is even more severe; the problem is reduced, without loss of generality, from 3D to 2D. To address pole singularities that arise in these coordinates and symmetric or anti-symmetric boundary conditions, we propose a generalization of the pole treatment method by Mohseni and Colonius [82] for scattered nodes. We introduce a set of ghost nodes, denoted as $\mathcal{X}^+$, which are symmetric to the interior nodes, $\mathcal{X}^\bullet$, with respect to the centerline. For each interior node, we divide its local stencil into two disjoint sets such that $\{x\}_{j=1}^n = \{x^\bullet_j\}_{j=1}^{n^\bullet} \cup \{x^+_j\}_{j=1}^{n^+}$, where $x^\bullet \in \mathcal{X}^\bullet$ and $x^+ \in \mathcal{X}^+$, respectively, and $n = n^\bullet + n^+$. Additionally, we define $\{x^\Delta_j\}_{j=1}^{n^+} \in \{x^\bullet_j\}_{j=1}^{n^\bullet}$ as the counterparts of the image nodes, and $\{x^\circ_j\}_{j=1}^{n^\bullet-n^+} = \{x^\bullet_j\}_{j=1}^{n^\bullet} \setminus \{x^\Delta_j\}_{j=1}^{n^+}$ represents the remaining nodes within the interior nodes, Refer to Fig. 3(b) for detailed symbol explanations. The function values at the image nodes are determined by their corresponding counterparts, given by

$$g(x^+_j) = \eta g(x^\Delta_j), \tag{37}$$

where η depends on the type of boundary conditions being imposed. Specifically, we use $\eta = 1$ for symmetric boundary conditions and $\eta = -1$ for anti-symmetric boundary conditions. The RBF-FD weights in equation (1) can be written as

$$Dg(x_0) = \sum_{j=1}^{n^\bullet} w^\bullet_j g(x^\bullet_j) + \sum_{j=1}^{n^+} w^+_j g(x^+_j) = \sum_{j=1}^{n^\bullet-n^+} w^\circ_j g(x^\circ_j) + \sum_{j=1}^{n^+} \left(\eta w^+_j + w^\Delta_j\right) g(x^\Delta_j). \tag{38}$$

This treatment allows us to approximate derivatives solely based on the function values at the interior nodes, effectively handling pole singularities and addressing the challenges associated with scattered nodes.

5. Applications

We demonstrate the mesh-free RBF-FD-based hydrodynamic stability framework outlined in §3 using three representative examples: canonical steady and unsteady cylinder wakes, a self-similar non-parallel steady laminar boundary-layer flow, and the turbulent mean of a transonic jet, as summarized in Table 3. These three examples are benchmark problems for open flows and are appropriate for validating mesh-free hydrodynamic stability.

5.1. Cylinder wake

We first consider the incompressible cylinder flow at diameter-based Reynolds numbers, $Re = \frac{U_\infty D}{\nu}$, ranging from 47 to 180 and investigate the mean-flow stability within the two-dimensional laminar regime. The occurrence of the periodic von Kármán vortex shedding in the cylinder wake beyond the critical Reynolds number of $Re_c \simeq 47$ is a well-known phenomenon, owing to

Table 3

Overview of datasets and analyses. The columns from left to right indicate the flow description, Reynolds number, Mach number, flow type, base state, analysis type, and section number. The zero-pressure-gradient (ZPG) Blasius solution is used for analyzing the boundary layer. Analyses include linear stability (LST) and resolvent analyses (RA), along with wavemaker (WM).

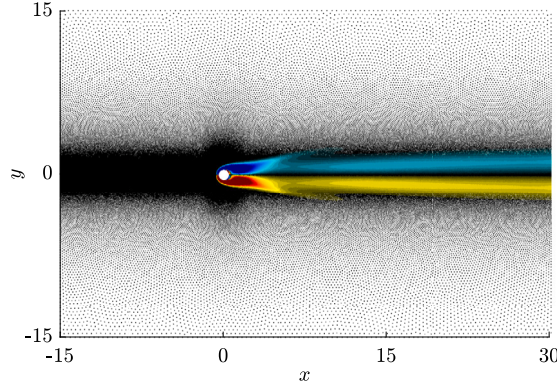| Flow	Re	M	Flow type	Base state	Analysis	Sec.
Cylinder wake [27]	$47-180$	-	2D laminar	$\overline{u}, \overline{v}$	LST/RA/WM	§5.1
Boundary layer (ZPG)	6×10^5	-	2D laminar	$u_{\mathrm{ZPG}}, v_{\mathrm{ZPG}}$	RA/WM	§5.2
Jet [21]	$\approx 10^6$	0.9	3D turbulent	$\overline{\rho}, \overline{u}_x, \overline{u}_r, \overline{u}_\theta, \overline{T}$	RA/WM	§5.3

Fig. 4. Computational grid for cylinder flows with $N = 118225$ nodes, colored using the mean vorticity, $\overline{\omega} = D_x \overline{v} - D_y \overline{u}$, at Re $= 100$.

a Hopf bifurcation that results in flow instability, see, e.g., [16,139]. Beyond the limit of Re $\simeq 188$, the cylinder flow becomes three-dimensional [11,143].

Classical LST analysis of the cylinder base flow ought to predict the onset of unsteadiness [54,147] but fails to capture the vortex-shedding frequency beyond Re$_c$ [10,119]. Previous studies by Hammond and Redekopp [46] and Pier [94] show that LST analysis around the cylinder mean flow accurately identifies the vortex-shedding frequency compared to experimental measurements. Barkley [10] supported these findings and showed that the cylinder mean flow is marginally stable in the 2D regime. Sipp and Marquet [119] subsequently provided theoretical underpinning by conducting a weakly nonlinear analysis and establishing criteria for utilizing mean flows in LST analysis. The vortex-shedding dynamics beyond the critical Reynolds number were later investigated using a self-consistent model [70,71] and RA [58,126] based on the mean flow stability. We here conduct both LST and resolvent analyses of the cylinder wake mean flow.

We define the computational domain Ω as the exterior of the cylinder $r \geq D/2 = 0.5$ and within the rectangle $-15 \leq x \leq 30$, $-15 \leq y \leq 15$. The computational domain is discretized using $N = 118225$ scattered nodes. Local grid refinement is employed near the cylinder with a characteristic distance of $\Delta r = 0.03$ and around the wake centerline with $\Delta r = 0.04$ to better resolve the flow structures. The unsteady cylinder flow is simulated using the PHS+poly RBF-FD version of the fractional-step, staggered-grid incompressible Navier-Stokes solver by Chu and Schmidt [27]. The mean-flow profiles are obtained as the time average of flow over 20 vortex-shedding cycles. Fig. 4 shows the mean vorticity at Re $= 100$ and the computational grid. Homogeneous boundary conditions, $u' = v' = 0$, are prescribed at the inlet and the cylinder surface. Symmetric boundary conditions with $v' = \partial u'/\partial y = 0$ are applied at the transverse boundaries. A stress-free outflow condition, $-p' \boldsymbol{n} + \frac{1}{\mathrm{Re}} \nabla \boldsymbol{u}' \cdot \boldsymbol{n} = 0$, where $\boldsymbol{n} = [1, 0]^T$ is the outflow direction, is enforced at the outflow.

The local wavemaker sensitivity in equation (24) and the resolvent gain in equation (27) and are both quantified in terms of the perturbed kinetic energy. To this end, we define the integration matrices

$$\boldsymbol{W}_u = \boldsymbol{W}_f \equiv \begin{bmatrix} \mathbf{1} & \mathbf{0} \\ \mathbf{0} & \mathbf{1} \end{bmatrix} \otimes \mathrm{diag}(\mathrm{d}V_1, \mathrm{d}V_2, \cdots, \mathrm{d}V_N) \tag{39}$$

in equation (28) to approximate the integral within the computational domain, where $\otimes$ denotes the Kronecker product. Here, $\mathrm{d}V_i = \xi \pi (\Delta r_i)^2$ is the local radial control volume for each grid. The constant ξ ensures consistency with the total control volume and is defined by letting $\sum_{i=1}^N \mathrm{d}V_i = \xi \pi \sum_{i=1}^N (\Delta r_i)^2 = \int_\Omega 1 \mathrm{d}\boldsymbol{x}$. Refer to Fig. 3 for practical illustrations.

Fig. 5 shows the Strouhal number, St $= \lambda_i/2\pi$, associated with the leading eigenvalues at varying Reynolds numbers. Starting from the critical Reynolds number of Re$_c \approx 47$, the frequency-Reynolds number dependence exhibits the typical features of a Hopf bifurcation. Our results are in good agreement with Barkley [10], and similarly, deviate no more than 3% from those reported by Pier [94]. The maximum growth rates are almost identical to zero (see also Fig. 6 below), confirming that the mean flow is marginally stable.

We next conduct a comparative study of LST and RA at two representative Reynolds numbers, the critical Reynolds number of Re $= 47$ and Re $= 100$, as an example of the unsteady regime. Fig. 6 shows the resulting resolvent singular value and stability
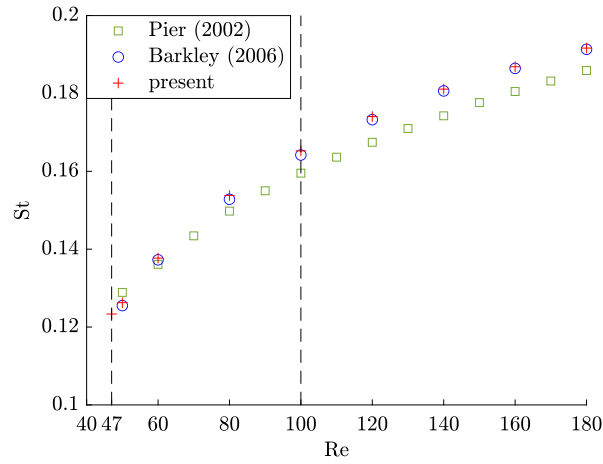
Fig. 5. Vortex shedding frequency predicted by the leading eigenvalue of the mean-flow stability problem as a function of Reynolds number. The frequency is given as the non-dimensional Strouhal number St $= \lambda_i/2\pi$. Shown for comparison are results from Pier [94] (green square) and Barkley [10] (blue circle). Two representative Reynolds numbers for the following analysis, $Re_c \approx 47$ and $Re = 100$, are highlighted as dashed lines.
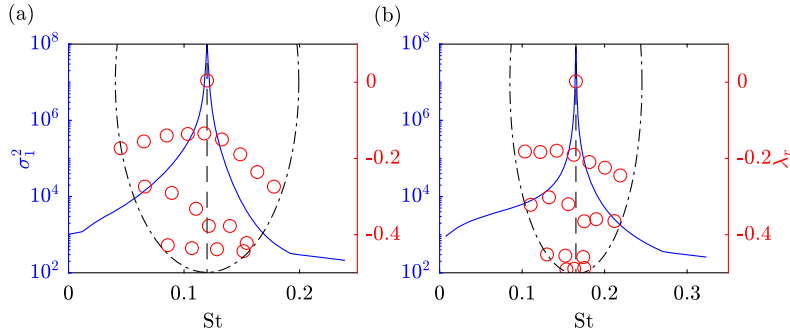

Fig. 6. Resolvent singular values (blue curve) and stability eigenvalue (red circle) spectra for $Re = 47$ (a) and $Re = 100$ (b). The 20 eigenvalues closest to $\lambda_c = 0 + 0.753i$ or $St_c = 0.1199$ and $\lambda = 0 + 1.038i$ or $St = 0.1652$ (dashed lines) were found within the regions outlined by the black dot-dashed lines using the shift-and-invert Arnoldi algorithm for $Re = 47$ and 100, respectively.

eigenvalue spectra. At $Re = Re_c$, both the peak of the resolvent gain and the leading eigenvalue identify the same frequency, $St_c = 0.1199$, as the vortex shedding frequency. This value is in good agreement with the results of the LST analysis around the base flow, see, e.g., Giannetti and Luchini [43] ($St_c \simeq 0.118$ for $Re_c \simeq 46.7$), Marquet et al. [72] ($St_c \simeq 0.116$ for $Re_c \simeq 46.8$), and Sipp and Marquet [119] ($St_c \simeq 0.118$ for $Re_c \simeq 46.6$). Similarly, the resolvent singular value spectrum at $Re = 100$ in panel 6(b) displays a clear peak at the vortex shedding frequency, which is now at $St = 0.1652$, and again coinciding with the least stable LST eigenvalue. This result matches closely with the findings of earlier Strouhal-Reynolds number relationship [35,57,70,95,143] and RA [58,126] studies.

Fig. 7 shows the leading LST and RA modes for the cylinder mean flow at $Re = Re_c$ and $Re = 100$. The leading LST and optimal response modes, along with their corresponding adjoint and forcing modes, are near-identical at both Reynolds numbers. The resemblance observed between the LST and resolvent response modes is to be anticipated, as the singular value of the resolvent attains its peak at the vortex-shedding frequency [17,126], thus exhibiting the characteristic vortex-shedding structure. This implies that the optimal forcing leverages the global instability mode to achieve maximum gain. Differing from the optimal response and LST modes, the optimal forcing and adjoint modes are active far upstream of the cylinder but peak downstream in close vicinity to the cylinder. This hallmark of convective instability was similarly observed in previous works [58,72,126].

We finally investigate the wavemaker ζ_{LST}, defined in equation (24), in Fig. 8 to quantify the sensitivity of spatially localized feedback. Wavemakers obtained from LST and RA look similar for both Reynolds numbers and reach their maxima in two symmetrically positioned lobes located across the separation bubble. This result signifies the promising applicability of RA-based wavemakers in accurately identifying the region where the flow instability mechanisms happen. The wavemaker patterns at the critical Reynolds number shown in panels 8 (a,c) compare well to those previously reported by Giannetti and Luchini [43] and Marquet et al. [72]. The shrinking of wavemaker region at $Re = 100$ in panels 8 (b,d) closely matches with the findings in Meliga et al. [78] and Symon et al. [126].
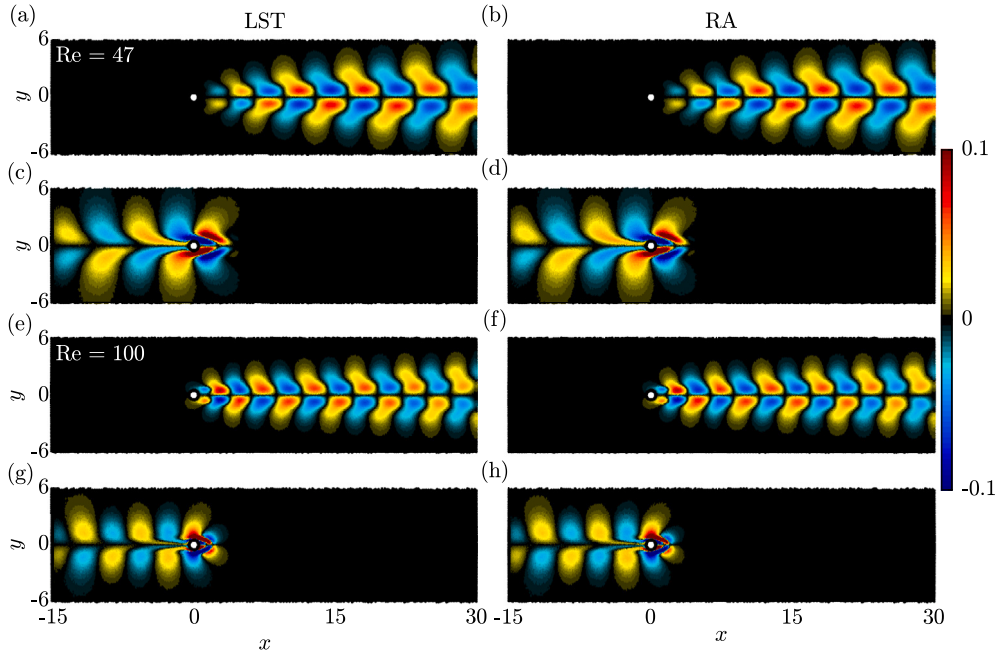
Fig. 7. Leading modes for Re = 47 at St = 0.1199 (a-d) and Re = 100 at St = 0.1652 (e-h): (a,e) LST modes; (b,f) response modes; (c,g) adjoint modes; (d,h) forcing modes.
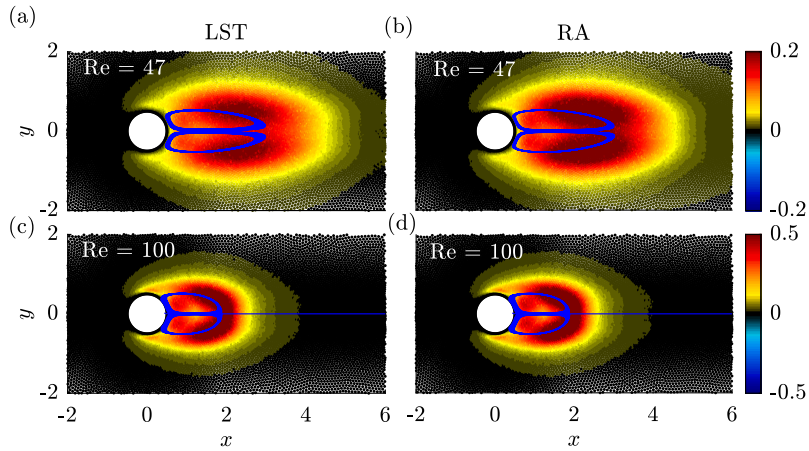

Fig. 8. Wavemakers ζ_{LST} for mean flow at (a) Re = 47 and (c) Re = 100. Respective results for ζ_{RA} are shown in (b) and (d). The blue curve represents the mean flow streamlines.

5.2. Blasius boundary layer

We now examine the incompressible two-dimensional non-normal flat-plate boundary layer, a classic example of convectively unstable flows characterized by the amplification of disturbances during downstream advection. The convective instability of boundary-layer flows has been extensively studied through 1D LST analysis over the past century, e.g., [60,68,69,100,124]. Above the critical displacement-thickness Reynolds number of $\mathrm{Re}_{\delta,c} \approx 520$, the Tollmien–Schlichting (TS) waves are known to arise as unstable eigenmodes of the Orr-Sommerfeld equation [23]. While these locally unstable waves are damped in 2D LST [1,2,6,32], investigations into the non-normality of the linearized Navier-Stokes equations for open flows have revealed an alternative pathway for disturbance amplification [25,73,121]. To analyze the non-modal behavior of boundary-layer flows, input-output analysis has been conducted to determine the optimal harmonic forcing that results in the largest asymptotic response [3,7,8,84,107,120].

Following the setup by Sipp and Marquet [120], we compute the resolvent gain in the restricted domain $\Omega_{\mathrm{RA}} = [x, y/\delta] \in [0.02, 1] \times [0, 22.52]$ within the computational domain $\Omega = [x, y/\delta] \in [0.02, 1.27] \times [0, 22.52]$ such that the forcing optimizes the ratio between the restricted kinetic energy, $\iint_{\Omega_{\mathrm{RA}}} \left(|\hat{u}|^2 + |\hat{v}|^2 \right) \mathrm{d}x\mathrm{d}y$, and the integral of forcing, $\iint_{\Omega} \left(|\hat{f}_u|^2 + |\hat{f}_v|^2 \right) \mathrm{d}x\mathrm{d}y$. The zero-pressure-gradient (ZPG) asymptotic Blasius solution, characterized by a local Reynolds number of $\mathrm{Re}_x = \frac{U_\infty x}{\nu} = 6 \times 10^5$ or $\mathrm{Re}_\delta = \frac{U_\infty \delta(x)}{\nu} = 1332$
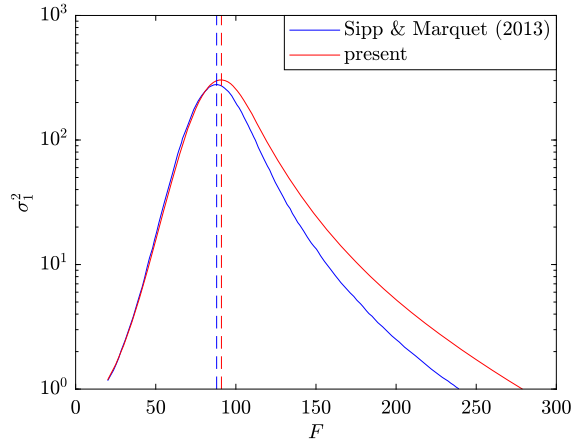
Fig. 9. Resolvent gains (solid lines) and peak frequencies (dashed lines) for the flat-plate boundary layer and $Re = 6 \cdot 10^5$.

at the end of the restricted domain Ω_{RA}, is used as the base flow to investigate the flow instabilities, where $\delta(x) = 1.72\sqrt{x/Re_x}$ is the displacement thickness. The leading edge ($x < 0.02$) is removed to avoid the singularity of the self-similar solution. Hereafter, we use the notations $Re = Re_{x=1}$ and $\delta = \delta(x = 1)$ for simplicity. Conversely, $x = 1$ in Figs. 10, 11, and 13 corresponds to $Re = 6 \times 10^5$. All quantities and coordinates presented are dimensionless.

The computational domain Ω is discretized using $N = 726143$ scattered nodes, corresponding to 2.2×10^6 degrees of freedom. In comparison, Sipp and Marquet [120] employ 13.7×10^6 degrees of freedom. The characteristic distances of the grid are $\Delta r = 0.069\delta$ near the flat plate ($y/\delta < 4$), $\Delta r = 0.077\delta$ near the inlet ($x < 0.025$), and average at 0.081δ over the whole domain. At the inlet and the flat plate, we prescribe $u' = v' = 0$. A symmetric boundary condition with $v' = \partial u'/\partial y = 0$ is applied at the far-field ($y/\delta = 22.52$). A stress-free outflow condition is enforced at the outflow. The weight matrix W_u is defined in equation (39), but with zero weights in the region $\Omega \setminus \Omega_{RA}$.

We first examine the leading resolvent singular value as a function of the normalized frequency, $F = 10^6 \cdot \omega/Re$, in Fig. 9. Overall, our results agree well with those reported by Sipp and Marquet [120]. The slight deviation of the peak and the resolvent gains beyond the peak ($F \gtrsim 88$) are most likely attributed to differences in the base flows, that is, the ZPG self-similar Blasius solution in the present study and the fully non-parallel numerical data of Sipp and Marquet [120] that includes the leading edge. The discrepancy at higher frequencies is potentially also related to the truncation of the leading edge, where the asymptotic Blasius solution becomes singular.

Fig. 10 shows the optimal and suboptimal forcings and corresponding responses at $F = 100$. The optimal response exhibits clear Tollmien–Schlichting (TS) wavepackets in the downstream region, while the upstream tilted structures in the optimal forcing highlight the active role of the Orr mechanism in extracting energy from the mean shear via the Reynolds stress [23]. The clear spatial separation between leading resolvent forcing and response modes indicates the stream-wise non-normality of the system [25,72,121]. The suboptimal forcing and response are similar to the leading modes except for two local maxima. This modulation confirms the orthogonality in their respective inner products. Qualitative comparisons with previous studies by Åkervik et al. [1], Monokrousos et al. [84], Brandt et al. [20] and Sipp and Marquet [120] verify the capability of the present framework in identifying the convective instability of the boundary-layer flow.

As a quantitative assessment of the flow structures, we examine the energy density functions,

$$d_f(x) = \int_0^{y_{max}} \left(|\hat{f}_u|^2 + |\hat{f}_v|^2 \right) \, dy, \qquad \text{and} \qquad d_u(x) = \int_0^{y_{max}} \left(|\hat{u}|^2 + |\hat{v}|^2 \right) \, dy, \tag{40}$$

in Fig. 11 for the modes shown in Fig. 10. Our results are almost identical to Sipp and Marquet [120] The spatial distribution of the optimal forcing unambiguously identifies the location of the upstream neutral point (branch I) from a local stability analysis at $x = 0.3$ and the corresponding response is localized at $x = 0.89$, which is in close proximity to the downstream neutral point (branch II).

Fig. 12 shows the energy density distributions of the optimal forcing and response as a function of frequency, with the stream-wise coordinate given in terms of the local Reynolds number, Re_δ. The optimal forcings agree well with Sipp and Marquet [120], and their maxima effectively delineate the convectively stable/unstable boundary (branch I) obtained using local stability theory. The Orr and TS mechanisms coexist and compete while both contribute to the overall energy gain of RA. As frequency increases, the spatial support of the TS-like optimal responses decreases, suggesting that the TS mechanism is only supported in a limited region of the shear layer at high frequencies. Additionally, the energy density of the forcing shows an increasing trend, indicating that the Orr mechanism becomes dominant at high frequencies. Similar to the deviation in the resolvent gain spectra shown in Fig. 9, we observe a slight downstream shift in the peak of optimal responses compared to the results reported Sipp and Marquet [120] for increasing frequency ($F \gtrsim 130$).
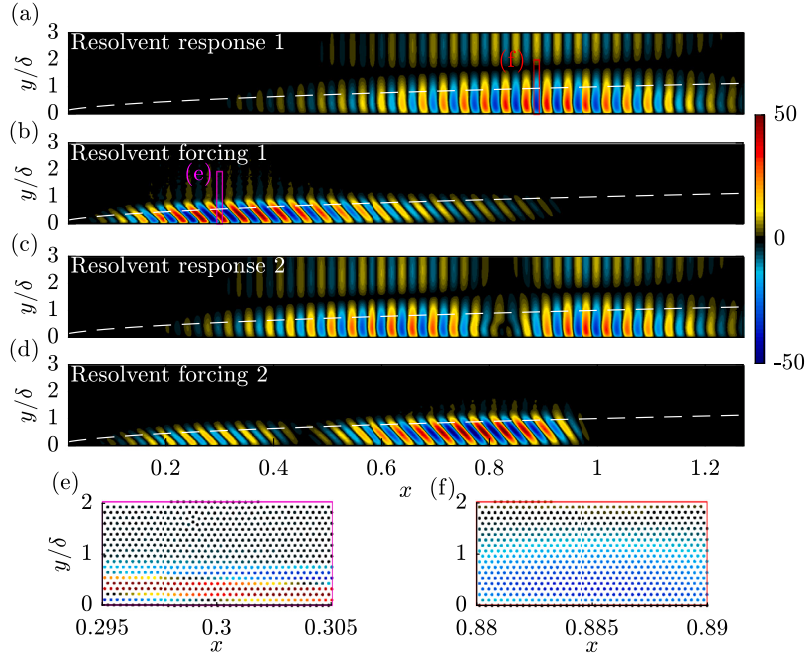
Fig. 10. Optimal and suboptimal resolvent forcings (b,d) and corresponding responses (a,c) for the flat-plate boundary layer at $F = 10^6 \cdot \omega/\mathrm{Re} = 100$. The normalized stream-wise velocity components have been interpolated onto a stretched Cartesian mesh for visualization. Panels (e) and (f) show the local regions of the optimal forcing (magenta box) and corresponding response modes (red box) with the largest magnitudes, respectively, on the scattered nodes used for the computation. The Blasius displacement thickness, $\delta(x)$, is highlighted as the white dashed line.
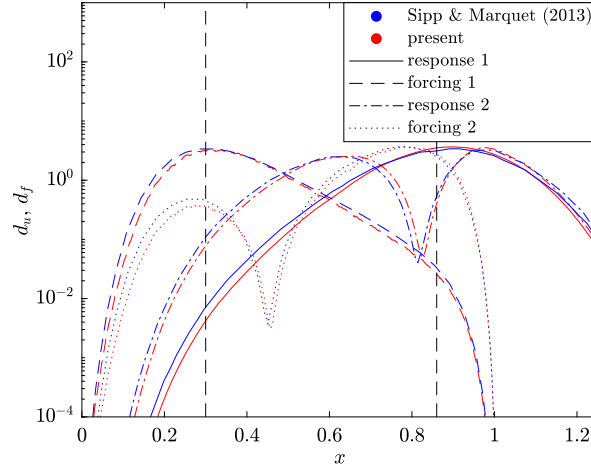

Fig. 11. Spatial distributions of energy density for optimal (dashed) and suboptimal (dotted) forcings and corresponding responses (solid and dot-dashed, respectively) at $F = 100$. The results (red) are compared to those reported by Sipp and Marquet [120] (blue). The two vertical solid lines represent the upstream neutral point (branch I) and the downstream neutral point (branch II) from a local stability analysis.

Finally, we show the RA-based wavemaker, defined in equation (32), in Fig. 13 to examine the instability mechanisms at different frequencies. The maximum magnitude of ζ_{RA} shows an increasing trend with frequency. The large magnitudes of the wavemaker are attributed to the fact that the value of the term $|\hat{u}_1^* W_u \hat{f}_1|^{-1}$ is considerably greater than the value of the self-adjoint modes, which is equal to 1 [73]. This again confirms that the boundary-layer flow exhibits high non-normality. For $F \lesssim 100$ (panels 13 (a-c)), the RA-based wavemaker exhibits an elongated shape and is artificially restricted within the optimization domain Ω_{RA}. The wavemaker becomes more concentrated towards the upstream region for higher frequencies ($F \gtrsim 140$, panels 13 (d-g)). This observation suggests a transition from the TS-dominated to the Orr-dominated mechanism as the frequency increases.
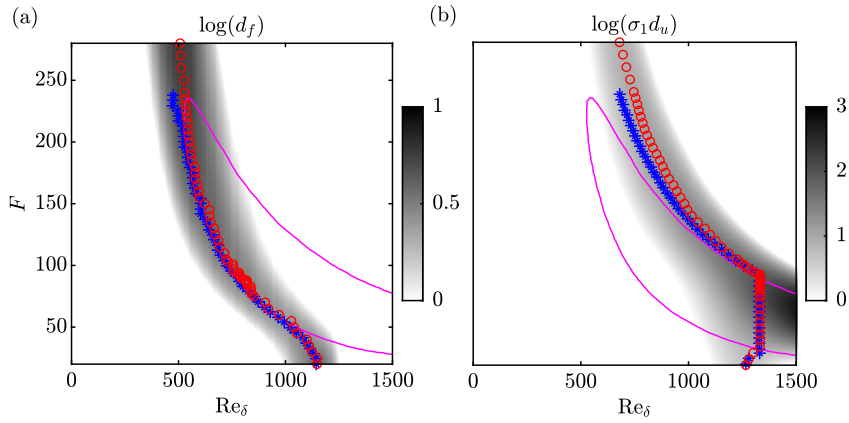
Fig. 12. Energy density distributions for the optimal forcings (a) and responses (b) as a function of frequency. The locations of maximum energy densities are marked as red circles. The results reported by Sipp and Marquet [120] are shown as blue stars for comparison. The neutral curve obtained from a local LST analysis is shown as the magenta line.
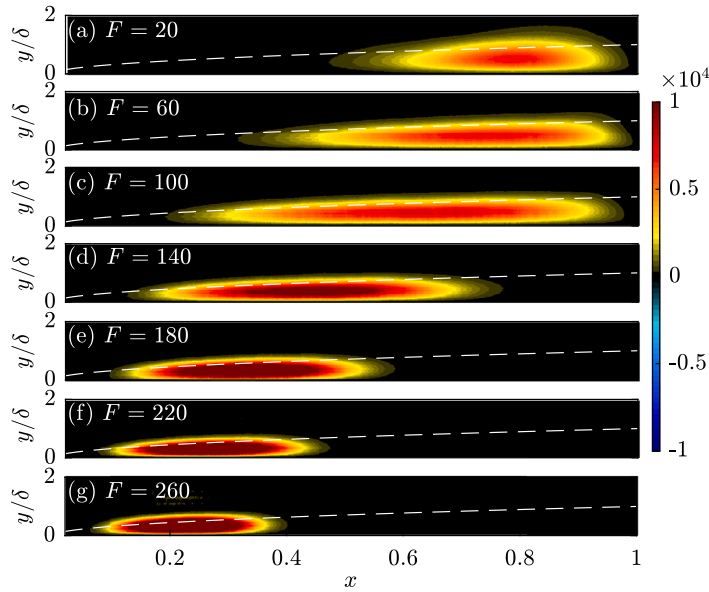

Fig. 13. RA-based wavemaker ζ_{RA} for the flat-plate boundary layer as a function of frequency.

5.3. Turbulent jet

The above two examples demonstrate the capability of the proposed numerical framework for analyzing incompressible flows within the laminar regime. We now focus on the mean flow analysis of a turbulent iso-thermal jet at Mach number, based on the jet velocity and the far-field speed of sound, of $M = 0.9$ and Reynolds number, based on the nozzle diameter and the jet velocity, of $\Re \approx 10^6$. The large eddy simulation (LES) data, generated using the unstructured flow solver 'Charles', is used for analysis. Further details about the dataset can be found in Brès et al. [21]. Previous studies have demonstrated that the transonic turbulent jet under consideration displays a variety of coherent features, including the well-known Kelvin–Helmholtz instabilities of the shear layer [21], downstream non-modal Orr-type waves [93,109], and trapped acoustic waves in the potential core [108,132].

The state vector,

$$q = [\rho, u_x, u_r, u_\theta, T]^T, \tag{41}$$

comprises primitive variables: density ρ, temperature T, and cylindrical velocity components u_x, u_r and u_θ in the streamwise, x, radial, r, and circumferential, θ, directions, respectively. The fluctuating state is defined as $q' = [\rho', u'_x, u'_r, u'_\theta, T']^T$. Owing to the rotational symmetry of the jet, we may decouple the governing equations and construct the compressible linear operator $\mathcal{L}$ in cylindrical coordinates, without loss of generality, for each azimuthal wavenumber m_θ independently. For a round jet, the mean azimuthal velocity component is zero. Upon linearization of the compressible Navier-Stokes equations shown in (A.1), we obtain the
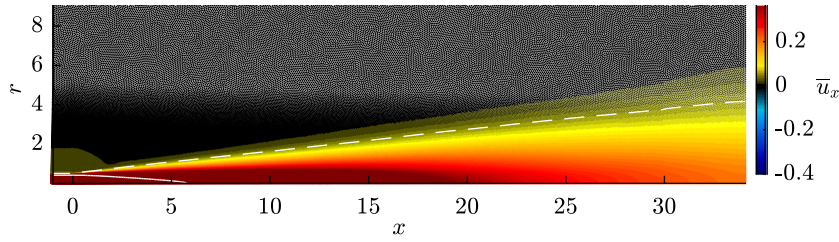
Fig. 14. Computational grid for jet with $N = 210817 \approx 1013 \times 208$ nodes, colored using the mean streamwise velocity $\overline{u}_x$ at Re $\approx 10^6$. The potential core (white solid) and the jet width (white dashed) are delineated as isolines corresponding to 99% and 5% of the jet velocity, respectively.
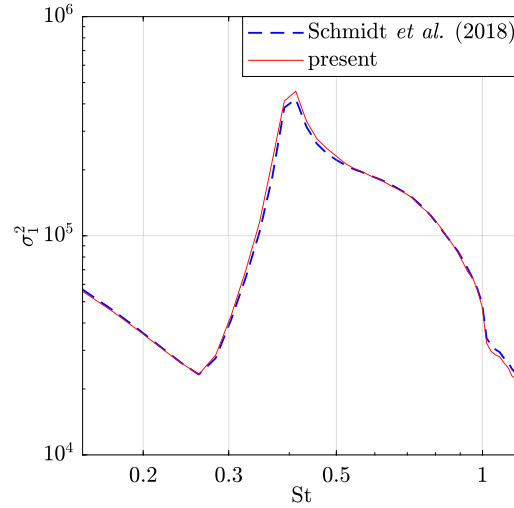

Fig. 15. Leading resolvent singular value spectra for the transonic jet and $m_\theta = 0$. Results reported by Schmidt et al. [109] are shown as comparisons (blue dashed).

linearized Navier-Stokes operator around the azimuthally averaged long-time mean of the primitive state, $\overline{q} = [\overline{\rho}, \overline{u}_x, \overline{u}_r, 0, \overline{T}]^T$, such that

$$\frac{\partial}{\partial t} q' = \mathcal{L} q' + f. \tag{42}$$

The general setup, including boundary conditions, sponge regions, and a molecular Reynolds number of Re $= 3 \times 10^4$, follows Schmidt et al. [108] and Schmidt et al. [109].

The computational domain $\Omega = [-1, 31.01] \times [0, 9.65]$ includes the physical domain $x, r \in [0, 30] \times [0, 6]$ and the surrounding sponge regions that prevent waves from being reflected. Local refinement is used near the nozzle with $\Delta r = 0.005$ and near the jet centerline with $\Delta r = 0.008$, resulting in $N = 210817$ scattered nodes for the construction of the RBF-FD-based global Jacobian L, see Fig. 14. A structured mesh with a comparable number of $N = 185250$ was used in Schmidt et al. [109].

The resolvent gain is quantified in terms of the compressible energy norm [26] through the weight matrices

$$\boldsymbol{W}_q = \boldsymbol{W}_f \equiv \text{diag}\left(\frac{\overline{T}}{\gamma \overline{\rho} M^2}, \overline{\rho}, \overline{\rho}, \overline{\rho}, \frac{\overline{\rho}}{\gamma(\gamma-1)\overline{T}M^2}\right) \otimes \text{diag}(2\pi r_1 \mathrm{d}V_1, 2\pi r_2 \mathrm{d}V_2, \cdots, 2\pi r_N \mathrm{d}V_N). \tag{43}$$

For compressible flows, the discrete weighted resolvent operator takes the form of

$$\boldsymbol{R}(\omega) = \boldsymbol{W}_q^{\frac{1}{2}} \boldsymbol{C} \left(\mathrm{i}\omega \boldsymbol{I} - \boldsymbol{L}\right)^{-1} \boldsymbol{B} \boldsymbol{W}_f^{-\frac{1}{2}}, \tag{44}$$

where the input and output matrices, $\boldsymbol{B}$ and $\boldsymbol{C}$, are used to are used to focus the analysis exclusively on the physical domain. As a first demonstration, we conduct the mesh-free RA for the symmetric component of the jet with $m_\theta = 0$ in the following.

Fig. 15 compares the leading resolvent singular value spectra to those reported by Schmidt et al. [109], obtained using a 4th-order finite difference [76] and a tenth-order filter for discretization. Very good agreement is observed within the frequency range $0.15 \lesssim \text{St} \lesssim 1.2$, with only a minor deviation at the peak value. This specific frequency range has been previously identified as the regime where different physical mechanisms are active in turbulent jets, see, e.g., [41,92,108,109,125,129,132].

To verify that large-scale coherent structures in the turbulent jet are accurately captured, we investigate the leading resolvent modes at three representative frequencies, as shown in Fig. 16. At St $= 0.2$, the optimal response exhibits a clear downstream ($x \gtrsim 10$) Orr-type wavepacket. The elongated structures tilted against the mean shear in the corresponding forcing are a clear
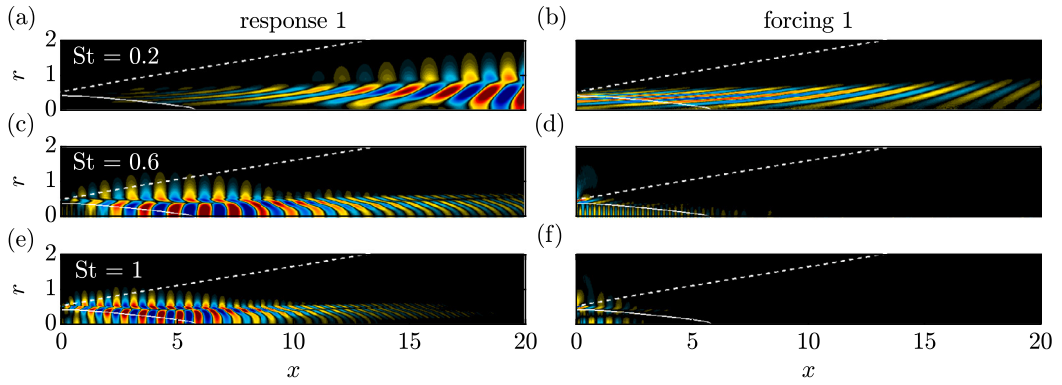
Fig. 16. Streamwise velocity component of the optimal response (a,c,e) and corresponding forcing modes (b,d,f) at three representative frequencies: (a-b) St = 0.2; (c-d) St = 0.6; (e-f) St = 1. The modes are interpolated onto a stretched Cartesian mesh with contours corresponding to $\pm 0.6 \| \cdot \|_\infty$ for visualization. The potential core and the jet width, shown in Fig. 14, are visualized for comparisons.
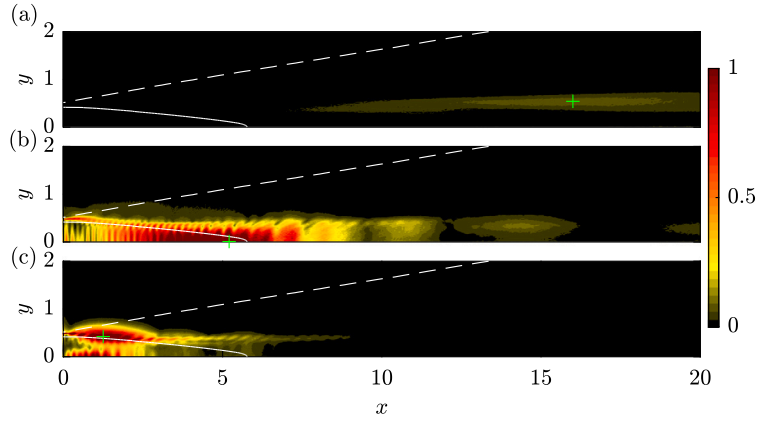

Fig. 17. RA-based wavemaker ζ_{RA} for: (a) St = 0.2; (b) St = 0.6; (c) St = 1. The region with the strongest feedback is marked as green '+'.

indicator of the Orr mechanism associated with the optimal non-modal spatial growth [109,128,129]. Similar flow structures have been reported in Garnaud et al. [41], Lesshafft et al. [66] and Pickering et al. [93]. For higher frequencies (St $\gtrsim$ 0.6), the optimal response take the form of compact Kelvin–Helmholtz (KH) wavepackets localized upstream in the initial shear layer region of the jet ($x \lesssim 10$), which can be identified as the modal KH-type shear-layer instability of the turbulent mean flow [45,59,125]. The corresponding forcing distributions near the lip line ($r \simeq 0.5$) remain indicative of the Orr mechanism, but this time with the KH instability [41,56,96,110,129]. Within the potential core, the optimal response exhibits duct modes at St = 0.6 and trapped acoustic waves at St = 1. The presence of the latter is a general feature of resonance mechanisms between propagating waves associated with the isothermal and transonic jet, as previously described in [108,132]. Notably, comparable patterns can be observed in the corresponding forcings, indicating the nearly self-adjoint nature of the trapped instability mechanism. We confirmed the modal shapes are almost identical to those obtained using the numerical scheme outlined in Schmidt et al. [109] (not shown).

Fig. 17 shows how the RA-based wavemaker, ζ_{RA}, unveils different physical mechanisms that are active in the turbulent jet. Most notably, the wavemaker region and its overall peak move upstream as the frequency increases from St = 0.2 to 1. At St = 0.2, the optimal forcing and response modes are spatially separated (see panels 16(a,b)), resulting in a very weak wavemaker signature in the downstream self-similar region. This result is anticipated, as the responses at low frequencies are purely triggered by the Orr mechanism without being associated with a single global mode or a local feedback mechanism that leads to the creation of waves in a localized region. This is indicative of a non-modal convective instability. At St = 0.6, the wavemaker peaks at the centerline at $x \simeq 5$. This is the end of the potential core, where upstream traveling acoustic modes are generated, also known as duct modes, as previously described by Towne et al. [132]. Parallel-flow models accurately predict the occurrence of duct modes, but the wavemaker potentially reveals the location where duct modes originate, which is not predicted by the theory. The wavemaker at St = 1 peaks within the shear layer, which is associated with the KH instability, but it also exhibits a comparable magnitude at the upstream region of the potential core, which identifies the resonance mechanisms that trigger trapped acoustic modes [108,132]. That is, the wavemaker analysis confirms the phase-linking between downstream KH waves and upstream traveling waves at St = 1. Note that this is not the case for St = 0.6, where the wavemaker is solely associated with the duct modes.

6. Summary and discussion

In this study, a novel higher-order mesh-free framework for hydrodynamic stability analysis is developed. The framework has been demonstrated and validated on three benchmark problems for open flows: a canonical laminar cylinder wake, a non-parallel flat-plate Blasius boundary layer, and a transonic turbulent jet. It also provides new insights into well-known physics. The proposed framework incorporates PHS-type RBFs with polynomial augmentations to discretize large hydrodynamic stability matrix problems on scattered nodes with high accuracy, stability, and computational efficiency. The resulting differentiation matrices are employed to construct the discrete linearized Navier-Stokes operator for conducting LST and RA. We propose a set of parameters to address the trade-off between accuracy and computational efficiency for PHS+Poly RBF-FD discretizations that provide best practices. In the context of scattered nodes, the practical implementations of various boundary conditions arising in hydrodynamic stability analysis are discussed and addressed.

The present mesh-free approach accurately predicts flow instabilities in wakes behind a 2D cylinder, including the vortex-shedding frequency, corresponding coherent structures, and structural sensitivity. The results are in good agreement with previous studies [10,43,72,94]. In the case of the Blasius boundary layer, the present framework accurately identifies the TS wavepackets and yields favorable quantitative and qualitative comparisons with those previously reported in the literature [1,20,84,120]. Furthermore, the RA-based wavemaker confirms the high non-normality of the boundary layer and the transition in dominant mechanisms from TS to Orr as the frequency increases. When applied to the mean flow of a turbulent jet, the mesh-free RA yields results that are almost identical to those reported by Schmidt et al. [109]. The application of RA-based WM analysis identifies distinct dominant physical mechanisms operating at different frequencies. These mechanisms include the Orr mechanism in the downstream region with a very weak wavemaker signature at $St = 0.2$, prominent duct-like structures near the end of the potential core at $St = 0.6$, and the phase coupling between the KH and trapped acoustic mechanisms at $St = 1$. These results closely align with the findings documented in prior literature, e.g., [59,66,108,109,132], and provide a new, global perspective on modal and non-modal growth in jets, as well as on the origins of these instabilities.

Building upon the pioneering work of Hardy [47], RBF discretizations have been widely employed in canonical problems, exhibiting a continual evolution through advancements like RBF-FDs [130] and PHS+poly RBFs [36]. More recently, this mesh-free approach has garnered attention in computational fluid dynamics (CFD) for physical exploration or engineering applications, see, e.g., [27,111–113,138]. While RBF-FDs demonstrate the capability to construct sparse differentiation operators, the potential applications in hydrodynamic stability analysis have not been thoroughly explored. The current work is the first demonstration of such applications. Future extensions encompass applications involving 3D and complex geophysical or engineering fluid flows.

CRediT authorship contribution statement

Tianyi Chu: Writing – original draft, Visualization, Validation, Software, Methodology, Investigation, Formal analysis, Data curation. **Oliver T. Schmidt:** Writing – review & editing, Supervision, Resources, Project administration, Methodology, Funding acquisition, Conceptualization.

Declaration of competing interest

The authors declare that they have no known competing financial interests or personal relationships that could have appeared to influence the work reported in this paper.

Data availability

Data will be made available on request.

Acknowledgements

Appendix A. Governing equations for compressible flows

The compressible Navier-Stokes equations govern the motion of a general, compressible Newtonian fluid,

$$
\begin{aligned}
\frac{\partial \rho}{\partial t} &= -\nabla \cdot \rho \mathbf{u}, \\
\frac{\partial \rho \mathbf{u}}{\partial t} &= -\frac{1}{2} \nabla \cdot (\mathbf{u} : \rho \mathbf{u} + \rho \mathbf{u} : \mathbf{u}) - \nabla p + \frac{1}{\mathrm{Re}} \nabla \cdot \boldsymbol{\tau}, \\
\frac{\partial \rho e}{\partial t} &= -\nabla \cdot \rho e \mathbf{u} + \frac{1}{(\gamma - 1)\mathrm{RePrMa}_\infty^2} \nabla \cdot k \nabla T - \nabla \cdot p \mathbf{u} + \frac{1}{\mathrm{Re}} \nabla \cdot \boldsymbol{\tau} \mathbf{u},
\end{aligned}
\tag{A.1}
$$

where, e is the total energy. For a Newtonian fluid, the viscous stress tensor is $\boldsymbol{\tau} = \mu \left(\nabla \mathbf{u} + \nabla \mathbf{u}^T \right) - \frac{2}{3} \mu (\nabla \cdot \mathbf{u}) \mathrm{I}$. All flow quantities are non-dimensionalized by their dimensional free-stream values, denoted by $(\cdot)_\infty^*$, and the coordinates by the jet diameter D.

The dimensionless Reynolds number $\text{Re} = \rho_\infty^* u_\infty^* D / \mu_\infty^*$, Prandtl number $\text{Pr} = c_p^* \mu_\infty^* / k_\infty^*$, and Mach number $M = u_\infty^* / a_\infty^*$ then fully describe the flow. Here, $\mu_\infty^*, k_\infty^*, c_p^*, \gamma, a_\infty^*$ are the free-stream values of the dynamic viscosity, heat conductivity, heat capacity at constant pressure, heat capacity ratio, and speed of sound, respectively. Closure of the equations is achieved under the assumption of an ideal gas, and using Sutherland's law to compute the dynamic viscosity from the local temperature.

References

[1] E. Åkervik, U. Ehrenstein, F. Gallaire, D.S. Henningson, Global two-dimensional stability measures of the flat plate boundary-layer flow, Eur. J. Mech. B, Fluids 27 (5) (2008) 501–513.

[2] F. Alizard, J.-C. Robinet, Spatially convective global modes in a boundary layer, Phys. Fluids 19 (11) (2007) 114105.

[3] F. Alizard, S. Cherubini, J.-C. Robinet, Sensitivity and optimal forcing response in separated boundary layer flows, Phys. Fluids 21 (6) (2009) 064108.

[4] F. Alizard, T. Gibis, B. Selent, U. Rist, C. Wenzel, Stochastic receptivity of laminar compressible boundary layers: an input-output analysis, Phys. Rev. Fluids 7 (7) (2022) 073902.

[5] H.J. Bae, S.T.M. Dawson, B.J. McKeon, Resolvent-based study of compressibility effects on supersonic turbulent boundary layers, J. Fluid Mech. 883 (2020) A29.

[6] S. Bagheri, E. Åkervik, L. Brandt, D.S. Henningson, Matrix-free methods for the stability and control of boundary layers, AIAA J. 47 (5) (2009) 1057–1068.

[7] S. Bagheri, L. Brandt, D.S. Henningson, Input–output analysis, model reduction and control of the flat-plate boundary layer, J. Fluid Mech. 620 (2009) 263–298.

[8] S. Bagheri, D.S. Henningson, J. Hoepffner, P.J. Schmid, Input-output analysis and control design applied to a linear model of spatially developing flows, Appl. Mech. Rev. 62 (2) (2009).

[9] S. Bagheri, P. Schlatter, P.J. Schmid, D.S. Henningson, J. Hoepffner, Global stability of a jet in crossflow, J. Fluid Mech. 624 (2009) 33–44, J. Fluid Mech. 624 (2009) 33–44.

[10] D. Barkley, Linear analysis of the cylinder wake mean flow, Europhys. Lett. 75 (5) (2006) 750.

[11] D. Barkley, R.D. Henderson, Three-dimensional Floquet stability analysis of the wake of a circular cylinder, J. Fluid Mech. 322 (1996) 215–241.

[12] V. Bayona, An insight into RBF-FD approximations augmented with polynomials, Comput. Math. Appl. 77 (9) (2019) 2337–2353.

[13] V. Bayona, Comparison of moving least squares and RBF+ poly for interpolation and derivative approximation, J. Sci. Comput. 81 (1) (2019) 486–512.

[14] V. Bayona, N. Flyer, B. Fornberg, G.A. Barnett, On the role of polynomials in RBF-FD approximations: II. Numerical solution of elliptic PDEs, J. Comput. Phys. 332 (2017) 257–273.

[15] V. Bayona, N. Flyer, B. Fornberg, On the role of polynomials in RBF-FD approximations: III. Behavior near domain boundaries, J. Comput. Phys. 380 (2019) 378–399.

[16] H. Bénard, The formation of gyration centres at the back of a moving obstacle, C. R. Acad. Sci. 147 (1908) 839–842.

[17] S. Beneddine, D. Sipp, A. Arnault, J. Dandois, L. Lesshafft, Conditions for validity of mean flow stability analysis, J. Fluid Mech. 798 (2016) 485–504.

[18] R. Betchov, A. Szewczyk, Stability of a shear layer between parallel streams, Phys. Fluids 6 (10) (1963) 1391–1396.

[19] N. Bonne, V. Brion, E. Garnier, R. Bur, P. Molton, D. Sipp, L. Jacquin, Analysis of the two-dimensional dynamics of a Mach 1.6 shock wave/transitional boundary layer interaction using a RANS based resolvent approach, J. Fluid Mech. 862 (2019) 1166–1202.

[20] L. Brandt, D. Sipp, J.O. Pralits, O. Marquet, Effect of base-flow variation in noise amplifiers: the flat-plate boundary layer, J. Fluid Mech. 687 (2011) 503–528.

[21] G.A. Brès, P. Jordan, V. Jaunet, M. Le Rallic, A.V.G. Cavalieri, A. Towne, S.K. Lele, T. Colonius, O.T. Schmidt, Importance of the nozzle-exit boundary-layer state in subsonic turbulent jets, J. Fluid Mech. 851 (2018) 83–124.

[22] B. Bugeat, J.-C. Chassaing, J.-C. Robinet, P. Sagaut, 3D global optimal forcing and response of the supersonic boundary layer, J. Comput. Phys. 398 (2019) 108888.

[23] K.M. Butler, B.F. Farrell, Three-dimensional optimal perturbations in viscous shear flow, Phys. Fluids A 4 (8) (1992) 1637–1650.

[24] A.V.G. Cavalieri, D. Rodríguez, P. Jordan, T. Colonius, Y. Gervais, Wavepackets in the velocity field of turbulent jets, J. Fluid Mech. 730 (2013) 559–592.

[25] J.-M. Chomaz, Global instabilities in spatially developing flows: non-normality and nonlinearity, Annu. Rev. Fluid Mech. 37 (2005) 357–392.

[26] B.-T. Chu, On the energy transfer to small disturbances in fluid flow (part 1), Acta Mech. 1 (3) (1965) 215–234.

[27] T. Chu, O. Schmidt, RBF-FD discretization of the Navier-Stokes equations on scattered but staggered nodes, J. Comput. Phys. 474 (2023) 111756.

[28] D.G. Crighton, M. Gaster, Stability of slowly diverging jet flow, J. Fluid Mech. 77 (2) (1976) 397–413.

[29] P. De, F. Miguel, D. Sipp, P.J. Schmid, Efficient evaluation of the direct and adjoint linearized dynamics from compressible flow solvers, J. Comput. Phys. 231 (23) (2012) 7739–7755.

[30] A. Dwivedi, G.S. Sidharth, M.R. Jovanović, Oblique transition in hypersonic double-wedge flow, J. Fluid Mech. 948 (2022) A37.

[31] A.D. Edstrand, P.J. Schmid, K. Taira, L.N. Cattafesta, A parallel stability analysis of a trailing vortex wake, J. Fluid Mech. 837 (2018) 858–895.

[32] U. Ehrenstein, F. Gallaire, On two-dimensional temporal modes in spatially evolving open flows: the flat-plate boundary layer, J. Fluid Mech. 536 (2005) 209–218.

[33] L.E. Eriksson, A. Rizzi, Computer-aided analysis of the convergence to steady state of discrete approximations to the Euler equations, J. Comput. Phys. 57 (1) (1985) 90–128.

[34] B.F. Farrell, P.J. Ioannou, Stochastic forcing of the linearized Navier–Stokes equations, Phys. Fluids A 5 (11) (1993) 2600–2609.

[35] U. Fey, M. König, H. Eckelmann, A new Strouhal–Reynolds-number relationship for the circular cylinder in the range $47 < \text{Re} < 2 \times 10^5$, Phys. Fluids 10 (7) (1998) 1547–1549.

[36] N. Flyer, G.A. Barnett, L.J. Wicker, Enhancing finite differences with radial basis functions: experiments on the Navier–Stokes equations, J. Comput. Phys. 316 (2016) 39–62.

[37] N. Flyer, B. Fornberg, V. Bayona, G.A. Barnett, On the role of polynomials in RBF-FD approximations: I. Interpolation and accuracy, J. Comput. Phys. 321 (2016) 21–38.

[38] B. Fornberg, T.A. Driscoll, G. Wright, R. Charles, Observations on the behavior of radial basis function approximations near boundaries, Comput. Math. Appl. 43 (3–5) (2002) 473–490.

[39] B. Fornberg, N. Flyer, Solving PDEs with radial basis functions, Acta Numer. 24 (2015) 215–258.

[40] B. Fornberg, E. Lehto, Stabilization of RBF-generated finite difference methods for convective PDEs, J. Comput. Phys. 230 (6) (2011) 2270–2285.

[41] X. Garnaud, L. Lesshafft, P.J. Schmid, P. Huerre, The preferred mode of incompressible jets: linear frequency response analysis, J. Fluid Mech. 716 (2013) 189–202.

[42] M. Gaster, E. Kit, I. Wygnanski, Large-scale structures in a forced turbulent mixing layer, J. Fluid Mech. 150 (1985) 23–39.

[43] F. Giannetti, P. Luchini, Structural sensitivity of the first instability of the cylinder wake, J. Fluid Mech. 581 (2007) 167–197.

[44] D. Gunderman, N. Flyer, B. Fornberg, Transport schemes in spherical geometries using spline-based RBF-FD with polynomials, J. Comput. Phys. 408 (2020) 109256.

[45] K. Gudmundsson, T. Colonius, Instability wave models for the near-field fluctuations of turbulent jets, J. Fluid Mech. 689 (2011) 97–128.

[46] D.A. Hammond, L.G. Redekopp, Global dynamics of symmetric and asymmetric wakes, J. Fluid Mech. 331 (1997) 231–260.

[47] R.L. Hardy, Multiquadric equations of topography and other irregular surfaces, J. Geophys. Res. 76 (8) (1971) 1905–1915.

[48] F. Hecht, New development in FreeFem++, J. Numer. Math. 20 (3–4) (2012) 251–266.

[49] C.-M. Ho, P. Huerre, Perturbed free shear layers, Annu. Rev. Fluid Mech. 16 (1) (1984) 365–422.

[50] P. Huerre, P.A. Monkewitz, Local and global instabilities in spatially developing flows, Annu. Rev. Fluid Mech. 22 (1) (1990) 473–537.

[51] Y. Hwang, C. Cossu, Amplification of coherent streaks in the turbulent Couette flow: an input–output analysis at low Reynolds number, J. Fluid Mech. 643 (2010) 333–348.

[52] J.L. Van Ingen, A suggested semi-empirical method for the calculation of the boundary layer transition region, Rep. UTHL-74, University of Technology, Dept. Aero. Engng., 1956.

[53] A. Iske, On the approximation order and numerical stability of local Lagrange interpolation by polyharmonic splines, in: W. Haussmann, K. Jetter, M. Reimer, J. Stöckler (Eds.), Modern Developments in Multivariate Approximation, in: International Series of Numerical Mathematics, Birkhäuser, Basel, 2003, pp. 153–165.

[54] C.P. Jackson, A finite-element study of the onset of vortex shedding in flow past variously shaped bodies, J. Fluid Mech. 182 (1987) 23–45.

[55] I. Jacobi, B.J. McKeon, Dynamic roughness perturbation of a turbulent boundary layer, J. Fluid Mech. 688 (2011) 258–296.

[56] J. Jeun, J.W. Nichols, M.R. Jovanović, Input-output analysis of high-speed axisymmetric isothermal jet noise, Phys. Fluids 28 (4) (2016) 047101.

[57] H. Jiang, L. Cheng, Strouhal–Reynolds number relationship for flow past a circular cylinder, J. Fluid Mech. 832 (2017) 170–188.

[58] B. Jin, S. Symon, S.J. Illingworth, Energy transfer mechanisms and resolvent analysis in the cylinder wake, Phys. Rev. Fluids 6 (2) (2021) 024702.

[59] P. Jordan, T. Colonius, Wave packets and turbulent jet noise, Annu. Rev. Fluid Mech. 45 (2013) 173–195.

[60] R. Jordinson, The flat plate boundary layer. Part 1. Numerical integration of the Orr—Sommerfeld equation, J. Fluid Mech. 43 (4) (1970) 801–811.

[61] M.R. Jovanović, B. Bamieh, Componentwise energy amplification in channel flows, J. Fluid Mech. 534 (2005) 145–183.

[62] E.J. Kansa, Multiquadrics—A scattered data approximation scheme with applications to computational fluid-dynamics—II solutions to parabolic, hyperbolic and elliptic partial differential equations, Comput. Math. Appl. 19 (8–9) (1990) 147–161.

[63] E. Larsson, E. Lehto, A. Heryudono, B. Fornberg, Stable computation of differentiation matrices and scattered node stencils based on Gaussian radial basis functions, SIAM J. Sci. Comput. 35 (4) (2013) 2096–2119.

[64] S. Le Borne, W. Leinen, Guidelines for RBF-FD discretization: numerical experiments on the interplay of a multitude of parameter choices, J. Sci. Comput. 95 (1) (2023) 8.

[65] S.K. Lele, Compact finite difference schemes with spectral-like resolution, J. Comput. Phys. 103 (1) (1992) 16–42.

[66] L. Lesshafft, O. Semeraro, V. Jaunet, A.V.G. Cavalieri, P. Jordan, Resolvent-based modeling of coherent wave packets in a turbulent jet, Phys. Rev. Fluids 4 (6) (2019) 063901.

[67] P. Luchini, A. Bottaro, Adjoint equations in stability analysis, Annu. Rev. Fluid Mech. 46 (2014) 493–517.

[68] M.L. Mack, A numerical study of the temporal eigenvalue spectrum of the Blasius boundary layer, J. Fluid Mech. 73 (3) (1976) 497–520.

[69] M.L. Mack, Boundary-layer linear stability theory, Technical Report No. AGARD-R-709, 1984.

[70] V. Mantič-Lugo, C. Arratia, F. Gallaire, Self-consistent mean flow description of the nonlinear saturation of the vortex shedding in the cylinder wake, Phys. Rev. Lett. 113 (8) (2014) 084501.

[71] V. Mantič-Lugo, C. Arratia, F. Gallaire, A self-consistent model for the saturation dynamics of the vortex shedding around the mean flow in the unstable cylinder wake, Phys. Fluids 27 (7) (2015) 074103.

[72] O. Marquet, D. Sipp, L. Jacquin, Sensitivity analysis and passive control of cylinder flow, J. Fluid Mech. 615 (2008) 221–252.

[73] O. Marquet, M. Lombardi, J.-M. Chomaz, D. Sipp, L. Jacquin, Direct and adjoint global modes of a recirculation bubble: lift-up and convective non-normalities, J. Fluid Mech. 622 (2009) 1–21.

[74] E. Martini, D. Rodríguez, A. Towne, A.V.G. Cavalieri, Efficient computation of global resolvent modes, J. Fluid Mech. 919 (2021) A3.

[75] G.E. Mattingly, W.O. Criminale, The stability of an incompressible two-dimensional wake, J. Fluid Mech. 51 (2) (1972) 233–272.

[76] K. Mattsson, J. Nordström, Summation by parts operators for finite difference approximations of second derivatives, J. Comput. Phys. 199 (2) (2004) 503–540.

[77] B.J. McKeon, A.S. Sharma, A critical-layer framework for turbulent pipe flow, J. Fluid Mech. 658 (2010) 336–382.

[78] P. Meliga, E. Boujo, F. Gallaire, A self-consistent formulation for the sensitivity analysis of finite-amplitude vortex shedding in the cylinder wake, J. Fluid Mech. 800 (2016) 327–357.

[79] D. Mirzaei, The direct radial basis function partition of unity (D-RBF-PU) method for solving PDEs, SIAM J. Sci. Comput. 43 (1) (2021) A54–A83.

[80] R. Moarref, M.R. Jovanović, Model-based design of transverse wall oscillations for turbulent drag reduction, J. Fluid Mech. 707 (2012) 205–240.

[81] R. Moarref, M.R. Jovanović, J.A. Tropp, A.S. Sharma, B.J. McKeon, A low-order decomposition of turbulent channel flow via resolvent analysis and convex optimization, Phys. Fluids 26 (5) (2014) 051701.

[82] K. Mohseni, T. Colonius, Numerical treatment of polar coordinate singularities, J. Comput. Phys. 157 (2) (2000) 787–795.

[83] P.A. Monkewitz, Subharmonic resonance, pairing and shredding in the mixing layer, J. Fluid Mech. 188 (1988) 223–252.

[84] A. Monokrousos, E. Åkervik, L. Brandt, D.S. Henningson, Global three-dimensional optimal disturbances in the Blasius boundary-layer flow using time-steppers, J. Fluid Mech. 650 (2010) 181–214.

[85] B.R. Noack, H. Eckelmann, A global stability analysis of the steady and periodic cylinder wake, J. Fluid Mech. 270 (1994) 297–330.

[86] K. Oberleithner, L. Rukes, J. Soria, Mean flow stability analysis of oscillating jet experiments, J. Fluid Mech. 757 (2014) 1–32.

[87] Y. Ohmichi, K. Yamada, Matrix-free triglobal adjoint stability analysis of compressible Navier–Stokes equations, J. Comput. Phys. 437 (2021) 110332.

[88] Ö. Oruç, A strong-form local meshless approach based on radial basis function-finite difference (RBF-FD) method for solving multi-dimensional coupled damped Schrödinger system appearing in Bose–Einstein condensates, Commun. Nonlinear Sci. Numer. Simul. 104 (2022) 106042.

[89] A. Peplinski, P. Schlatter, D.S. Henningson, Global stability and optimal perturbation for a jet in cross-flow, Eur. J. Mech. B, Fluids 949 (2015) 438–447.

[90] P.O. Persson, Ph.D. thesis, Massachusetts Institute of Technology, 2005.

[91] J.-L. Pfister, N. Fabbiane, O. Marquet, Global stability and resolvent analyses of laminar boundary-layer flow interacting with viscoelastic patches, J. Fluid Mech. 937 (2022) A1.

[92] E. Pickering, G. Rigas, P.A.S. Nogueira, A.V.G. Cavalieri, O.T. Schmidt, T. Colonius, Lift-up, Kelvin–Helmholtz and Orr mechanisms in turbulent jets, J. Fluid Mech. 896 (2020) A2.

[93] E. Pickering, G. Rigas, O.T. Schmidt, D. Sipp, T. Colonius, Optimal eddy viscosity for resolvent-based models of coherent structures in turbulent jets, J. Fluid Mech. 917 (2021) A29.

[94] B. Pier, On the frequency selection of finite-amplitude vortex shedding in the cylinder wake, J. Fluid Mech. 458 (2002) 407–417.

[95] F.L. Ponta, H. Aref, Strouhal-Reynolds number relationship for vortex streets, Phys. Rev. Lett. 93 (8) (2004) 084501.

[96] U.A. Qadri, P.J. Schmid, Effect of nonlinearities on the frequency response of a round jet, Phys. Rev. Fluids 2 (4) (2017) 043902.

[97] Z. Qian, L. Wang, C. Zhang, Z. Zhong, Q. Chen, Conservation and accuracy studies of the LESCM for incompressible fluids, J. Comput. Phys. (2017) 112269.

[98] S.C. Reddy, D.S. Henningson, Energy growth in viscous channel flows, J. Fluid Mech. 252 (1993) 209–238.

[99] S.C. Reddy, P.J. Schmid, D.S. Henningson, Pseudospectra of the Orr–Sommerfeld operator, SIAM J. Appl. Math. 53 (1) (1993) 15–47.

[100] H.L. Reed, W.S. Saric, D. Arnal, Linear stability theory applied to boundary layers, Annu. Rev. Fluid Mech. 28 (1) (1996) 389–428.

[101] M.A. Regan, K. Mahesh, Global linear stability analysis of jets in cross-flow, J. Fluid Mech. 828 (2017) 812–836.

[102] J.H.M. Ribeiro, C.-A. Yeh, K. Taira, Randomized resolvent analysis, Phys. Rev. Fluids 5 (3) (2020) 033902.

[103] J.H.M. Ribeiro, C.-A. Yeh, K. Zhang, K. Taira, Wing sweep effects on laminar separated flows, J. Fluid Mech. 950 (2022) A23.

[104] G. Rigas, D. Sipp, T. Colonius, Nonlinear input/output analysis: application to boundary layer transition, J. Fluid Mech. 911 (2021) A15.

[105] K. Rosenberg, B.J. McKeon, Computing exact coherent states in channels starting from the laminar profile: a resolvent-based approach, Phys. Rev. E 100 (2) (2019) 021101.

[106] L.G.C. Santos, N. Manzanares-Filho, G.J. Menon, E. Abreu, Comparing RBF-FD approximations based on stabilized Gaussians and on polyharmonic splines with polynomials, Int. J. Numer. Methods Eng. 115 (4) (2018) 462–500.

[107] P.J. Schmid, D.S. Henningson, Stability and Transition in Shear Flows, Springer, 2001.

[108] O.T. Schmidt, A. Towne, T. Colonius, A.V. Cavalieri, P. Jordan, G.A. Brès, Wavepackets and trapped acoustic modes in a turbulent jet: coherent structure eduction and global stability, J. Fluid Mech. 825 (2017) 1153–1181.

[109] O.T. Schmidt, A. Towne, G. Rigas, T. Colonius, G.A. Brès, Spectral analysis of jet turbulence, J. Fluid Mech. 855 (2018) 953–982.

[110] O. Semeraro, L. Lesshafft, V. Jaunet, P. Jordan, Modeling of coherent structures in a turbulent jet as global linear instability wavepackets: theory and experiment, Int. J. Heat Fluid Flow 62 (2016) 24–32.

[111] S. Shahane, A. Radhakrishnan, S.P. Vanka, A high-order accurate meshless method for solution of incompressible fluid flow problems, J. Comput. Phys. 445 (2021) 110623.

[112] S. Shahane, S.P. Vanka, Consistency and convergence of a high order accurate meshless method for solution of incompressible fluid flows, preprint, arXiv: 2202.02828.

[113] S. Shahane, S.P. Vanka, A semi-implicit meshless method for incompressible flows in complex geometries, J. Comput. Phys. 472 (2023) 111715.

[114] V. Shankar, The overlapped radial basis function-finite difference (RBF-FD) method: a generalization of RBF-FD, J. Comput. Phys. 342 (2017) 211–228.

[115] V. Shankar, A.L. Fogelson, Hyperviscosity-based stabilization for radial basis function-finite difference (RBF-FD) discretizations of advection–diffusion equations, J. Comput. Phys. 372 (2018) 616–639.

[116] A.S. Sharma, B.J. McKeon, On coherent structure in wall turbulence, J. Fluid Mech. 728 (2013) 196–238.

[117] G.S. Sidharth, A. Dwivedi, G.V. Candler, J.W. Nichols, Onset of three-dimensionality in supersonic flow over a slender double wedge, Phys. Rev. Fluids 3 (9) (2018) 093901.

[118] D. Sipp, Open-loop control of cavity oscillations with harmonic forcings, J. Fluid Mech. 708 (2012) 439–468.

[119] D. Sipp, A. Lebedev, Global stability of base and mean flows: a general approach and its applications to cylinder and open cavity flows, J. Fluid Mech. 593 (2007) 333–358.

[120] D. Sipp, O. Marquet, Characterization of noise amplifiers with global singular modes: the case of the leading-edge flat-plate boundary layer, Theor. Comput. Fluid Dyn. 27 (5) (2013) 617–635.

[121] D. Sipp, O. Marquet, P. Meliga, A. Barbagallo, Dynamics and control of global instabilities in open-flows: a linearized approach, Appl. Mech. Rev. 63 (3) (2010).

[122] C.S. Skene, C.-A. Yeh, P.J. Schmid, K. Taira, Sparsifying the resolvent forcing mode via gradient-based optimisation, J. Fluid Mech. 944 (2022) A52.

[123] A.M.O. Smith, N. Gamberoni, Transition, pressure gradient and stability theory, Rep. ES 26388, Douglas Aircraft Co., El Segundo, CA, 1956.

[124] F.T. Smith, On the non-parallel flow stability of the Blasius boundary layer, Proc. R. Soc. Lond. Ser. A 366 (1724) (1979) 91–109.

[125] T. Suzuki, T. Colonius, Instability waves in a subsonic round jet detected using a near-field phased microphone array, J. Fluid Mech. 565 (2006) 197–226.

[126] S. Symon, K. Rosenberg, S.T.M. Dawson, B.J. McKeon, Non-normality and classification of amplification mechanisms in stability and resolvent analysis, Phys. Rev. Fluids 3 (5) (2018) 053902.

[127] V. Theofilis, Global linear instability, Annu. Rev. Fluid Mech. 43 (2011) 319–352.

[128] G. Tissot, F.C. Lajús Jr., A.V.G. Cavalieri, P. Jordan, Wave packets and Orr mechanism in turbulent jets, Phys. Rev. Fluids 2 (9) (2017) 093901.

[129] G. Tissot, M. Zhang, F.C. Lajús Jr., A.V.G. Cavalieri, P. Jordan, Sensitivity of wavepackets in jets to nonlinear effects: the role of the critical layer, J. Fluid Mech. 811 (2017) 95–137.

[130] A.I. Tolstykh, On using RBF-based differencing formulas for unstructured and mixed structured-unstructured grid calculations, in: Proc. 16th IMACS World Congress, vol. 228, 2000, pp. 4606–4624.

[131] I. Tominec, E. Larsson, A. Heryudono, A least squares radial basis function finite difference method with improved stability properties, SIAM J. Sci. Comput. 43 (2) (2021) A1441–A1471.

[132] A. Towne, A. Cavalieri, P. Jordan, T. Colonius, O.T. Schmidt, V. Jaunet, G. Brès, Acoustic resonance in the potential core of subsonic jets, J. Fluid Mech. 825 (2017) 1113–1152.

[133] A. Towne, G. Rigas, O. Kamal, E. Pickering, T. Colonius, Efficient global resolvent analysis via the one-way Navier–Stokes equations, J. Fluid Mech. 948 (2022) A9.

[134] A. Towne, O.T. Schmidt, T. Colonius, Spectral proper orthogonal decomposition and its relationship to dynamic mode decomposition and resolvent analysis, J. Fluid Mech. 847 (2018) 821–867.

[135] L.N. Trefethen, A.E. Trefethen, S.C. Reddy, T.A. Driscoll, Hydrodynamic stability without eigenvalues, Science 261 (5121) (1993) 578–584.

[136] L. Tuckerman, D. Barkley, Bifurcation analysis for timesteppers, in: Numerical Methods for Bifurcation Problems and Large-Scale Dynamical Systems, 2000, pp. 453–466.

[137] L. Tuckerman, P. Marcus, Formation of Taylor vortices in spherical Couette flow, in: Ninth Int'l Conf on Numerical Methods in Fluid Dynamics, 1985, pp. 552–556.

[138] A. Unnikrishnan, S. Shahane, V. Narayan, S.P. Vanka, Shear-driven flow in an elliptical enclosure generated by an inner rotating circular cylinder, Phys. Fluids 34 (1) (2022) 013607.

[139] T. Vón Kármán, Über den Mechanismus des Widerstandes, den ein bewegter Körper in einer Flüssigkeit erfährt, Gött. Nachr. Math. Phys. Kl. 1911 (1911) 509–517.

[140] L. Wang, Radial basis functions methods for boundary value problems: performance comparison, Eng. Anal. Bound. Elem. 84 (2017) 191–205.

[141] L. Wang, Z. Qian, Y. Zhou, Y. Peng, A weighted meshfree collocation method for incompressible flows using radial basis functions, J. Comput. Phys. 401 (2020) 108964.

[142] I. Weisbrot, I. Wygnanski, On coherent structures in a highly excited mixing layer, J. Fluid Mech. 195 (1988) 137–159.

[143] C.H.K. Williamson, Vortex dynamics in the cylinder wake, Annu. Rev. Fluid Mech. 28 (1) (1996) 477–539.

[144] B.M. Woodley, N. Peake, Global linear stability analysis of thin aerofoil wakes, J. Fluid Mech. 339 (1997) 239–260.

[145] G.B. Wright, B. Fornberg, Scattered node compact finite difference-type formulas generated from radial basis functions, J. Comput. Phys. 212 (1) (2006) 99–123.

[146] C.-A. Yeh, K. Taira, Resolvent-analysis-based design of airfoil separation control, J. Fluid Mech. 867 (2019) 572–610.

[147] A. Zebib, Stability of viscous flow past a circular cylinder, J. Eng. Math. 21 (2) (1987) 155–165.